



1 Satellite-based radiative forcing by light-absorbing particles in snow across the  
2 Northern Hemisphere

3

4 Jiecan Cui<sup>1</sup>, Tenglong Shi<sup>1</sup>, Yue Zhou<sup>1</sup>, Dongyou Wu<sup>1</sup>, Xin Wang<sup>1,2</sup> and Wei Pu<sup>1</sup>

5 <sup>1</sup>Key Laboratory for Semi-Arid Climate Change of the Ministry of Education, College  
6 of Atmospheric Sciences, Lanzhou University, Lanzhou 730000, China

7 <sup>2</sup>Institute of Surface-Earth System Science, Tianjin University, Tianjin 300072, China

8

9 Corresponding author: Wei Pu ([puw09@lzu.edu.cn](mailto:puw09@lzu.edu.cn)) and Xin Wang ([wxin@lzu.edu.cn](mailto:wxin@lzu.edu.cn))

10



1 **Abstract.** Snow is the most reflective natural surface on Earth and consequently plays  
2 an important role in Earth's climate. Light-absorbing particles (LAPs) deposited on the  
3 snow surface can effectively decrease snow albedo, resulting in positive radiative  
4 forcing. In this study, we used remote sensing data from NASA's Moderate Resolution  
5 Imaging Spectroradiometer (MODIS) and the Snow, Ice, and Aerosol Radiative  
6 (SNICAR) model to quantify the reduction in snow albedo due to LAPs, before  
7 validating and correcting the data against *in situ* observations. We then incorporated  
8 these corrected albedo-reduction data in the Santa Barbara DISORT Atmospheric  
9 Radiative Transfer (SBDART) model to estimate Northern Hemisphere radiative  
10 forcing in January and February for the period 2003–2018. Our analysis reveals an  
11 average corrected reduction in snow albedo ( $\Delta\alpha_{MODIS,corrected}^{LAPs}$ ) of  $\sim 0.0246$ , with  
12 instantaneous radiative forcing ( $RF_{MODIS,ins}^{LAPs}$ ) and daily radiative forcing ( $RF_{MODIS,daily}^{LAPs}$ )  
13 values of  $\sim 5.9$  and  $\sim 1.7$  W m<sup>-2</sup>, respectively. We also observed significant spatial  
14 variations in  $\Delta\alpha_{MODIS,corrected}^{LAPs}$ ,  $RF_{MODIS,ins}^{LAPs}$ , and  $RF_{MODIS,daily}^{LAPs}$  throughout the  
15 Northern Hemisphere, with the lowest respective values ( $\sim 0.0123$ ,  $\sim 1.1$  W m<sup>-2</sup>, and  
16  $\sim 0.29$  W m<sup>-2</sup>) occurring in the Arctic and the highest ( $\sim 0.1669$ ,  $\sim 36$  W m<sup>-2</sup>, and  $\sim 11$   
17 W m<sup>-2</sup>) in northeastern China. From MODIS retrievals, we determined that the LAP  
18 content of snow accounts for 57.6% and 37.2% of the spatial variability in Northern  
19 Hemisphere albedo reduction and radiative forcing, respectively. We also compared  
20 retrieved radiative forcing values with those of earlier studies, including local-scale  
21 observations, remote-sensing retrievals, and model-based estimates. Ultimately,



1 estimates of radiative forcing based on satellite-retrieved data are shown to represent  
2 true conditions on both regional and global scales.

3

#### 4 **1. Introduction**

5 Seasonal snow cover affects 30% of Earth's land surface and exerts a cooling influence  
6 on global climate through its direct interaction with the surface radiation budget  
7 (Painter et al., 1998; Flanner et al., 2011). However, snow surface darkening due to  
8 light-absorbing particles (LAPs) such as black carbon (BC), organic carbon (OC), dust,  
9 and algae, can significantly alter the reflective properties of snow (Warren, 1982, 1984;  
10 Hadley and Kirchstetter, 2012). When deposited on the snow surface, LAPs increase  
11 the absorption of solar radiation (Painter et al., 2012a; Liou et al., 2014; Dang, 2017),  
12 thereby reducing the snow albedo (Warren and Brandt, 2008; Kaspari et al., 2014). As  
13 a result, radiative forcing of LAPs in snow (RFLS) plays a critical role in snow-cover  
14 decline on both regional and global scales (Warren and Wiscombe, 1980), perturbing  
15 the climate system and impacting hydrological cycles (Qian et al., 2011).

16 One of the primary LAPs, BC, is derived from the incomplete combustion of fossil  
17 fuels and biomass (Bond et al., 2013; Dang et al., 2015) and is second only to CO<sub>2</sub> in  
18 its contribution to climate forcing (Hansen and Nazarenko, 2004; Ramanathan and  
19 Carmichael, 2008; Bond et al., 2013). Yet, despite considerable efforts to measure the  
20 BC content of Northern Hemisphere snow and ice (Doherty et al., 2010, 2014; Huang  
21 et al., 2011; Ye et al., 2012; Wang et al., 2013b, 2017), the inherent challenges presented



1 by a temporospatially variable snow cover mean our understanding of LAPs in snow is  
2 far from complete. As a result, RFLS estimate based on field measurements remains a  
3 persistent uncertainty in regional and global scale (Zhao et al., 2014).

4 Several previous investigations have utilized numerical models to estimate RFLS,  
5 including that of Hansen and Nazarenko (2004), who concluded that BC in snow and  
6 ice exerts a positive climate forcing throughout the Northern Hemisphere of +0.3  
7  $\text{W m}^{-2}$ , or approximately one quarter of observed global warming. More recently,  
8 Flanner et al. (2007) employed an aerosol/chemical-transport general-circulation model,  
9 coupled with the Snow, Ice, and Aerosol Radiative (SNICAR) model (Flanner et al.,  
10 2007; 2009), to estimate globally averaged radiative forcing values of +0.054 (range  
11 0.007–0.13) and +0.049 (0.007–0.12)  $\text{W m}^{-2}$  for a strong (1998) and weak (2001) boreal  
12 fire year, respectively. Using the Weather Research and Forecasting (WRF) model  
13 (Skamarock et al., 2008) coupled with a chemistry component (Chem) (Grell et al.,  
14 2005) and SNICAR modeling, Zhao et al. (2014) demonstrated that RFLS over northern  
15 China in January–February 2010 was  $\sim 10 \text{ W m}^{-2}$ . However, despite their potentially  
16 valuable contribution, climate models contain significant uncertainties in  
17 representations of LAP emissions, transport, deposition, and post-depositional  
18 processes that can propagate into simulations of LAP concentrations and their climate  
19 forcing (Qian et al., 2015; Lee et al., 2016). Zhao et al. (2014) also confirmed that,  
20 relative to observational data, modeled LAPs and radiative forcing estimates exhibit  
21 biases that are difficult to explain and quantify. These shortcomings underscore the need



1 for a refined approach to estimating real-time RFLS that minimizes the mismatch  
2 between field observations and model simulations.

3 In addition to modeling, remote sensing has been used to assess the physical  
4 characteristics of snow cover (Nolin and Dozier, 1993, 2000; Painter et al., 2009, 2012a,  
5 2013; Miller et al., 2016). Nolin and Dozier (2000), for example, retrieved grain-size  
6 data from satellite-derived reflectance at near-infrared (NIR) wavelengths, following  
7 the rationale that snow-grain size, in conjunction with solar zenith angle, dictates the  
8 path-length of penetrating photons (Wiscombe and Warren, 1980) and thus influences  
9 albedo in the NIR. Similarly, recent studies have attempted to employ satellite-derived  
10 snow albedo at visible (VIS) wavelengths to retrieve RFLS data (Seidel et al., 2016; Pu  
11 et al., 2019). Briefly, this retrieval method exploits the imaginary component of the  
12 complex refractive index for ice ( $K_{ice}$ ), which is very low at VIS wavelengths and  
13 results in the extremely high VIS albedo for pure snow. In contrast, the imaginary  
14 component of the complex refractive index for LAPs ( $K_{LAPs}$ ) at VIS wavelengths is  
15 orders of magnitude greater, resulting in the reduction in VIS snow albedo (Wiscombe  
16 and Warren, 1980). Moreover, albedo variability at VIS wavelengths is dominated by  
17 even minor concentrations of LAPs (Brandt et al., 2011; Painter et al., 2012b).

18 Painter et al. (2012a) employed surface-reflectance data provided by NASA's Moderate  
19 Resolution Imaging Spectroradiometer (MODIS) for the Upper Colorado River Basin  
20 and Hindu Kush-Himalaya (HKH) to make the first quantitative, remote-sensing-based  
21 retrievals of instantaneous surface radiative forcing (RF) due to LAPs. Relative to the



1 Western Energy Balance of Snow (WEBS) network (Painter et al., 2007), that study  
2 established that MODIS-derived radiative forcing exhibits a positive bias at lower RF  
3 values and a slightly negative bias at higher values. A more recent study by Seidel et al.  
4 (2016) used remote sensing to constrain instantaneous melt-season RFLS values of 20–  
5 200 W m<sup>-2</sup> for the Sierra Nevada and Rocky Mountains, while Pu et al. (2019) reported  
6 MODIS-derived values of 22–65 W m<sup>-2</sup> for northern China in January–February  
7 (regional average ~45 W m<sup>-2</sup>). Acknowledging this demonstrated efficacy of remote  
8 sensing retrievals for establishing RFLS on regional scales, we note this approach has  
9 so far not captured spatial variability in RFLS on a global scale.

10 In this study, we employed MODIS data to determine the reduction in Northern  
11 Hemisphere snow albedo due to LAPs. Retrievals were validated and corrected  
12 according to ground-based snow observations, after which spatial variability in albedo  
13 reduction and radiative forcing were assessed quantitatively. Finally, we compared our  
14 satellite-derived radiative forcing values with the results of a Global Climate Model  
15 (GCM) (Flanner et al., 2009) and the Coupled Model Intercomparison Project Phase 6  
16 (CMIP6) (Eyring et al., 2016). Despite the persistence of non-negligible uncertainties  
17 and biases, our satellite-based retrievals constitute the first hemisphere-scale  
18 assessment of RFLS and provide valuable parameters for improving climate model  
19 simulations.

20

## 21 **2. Data**



## 1 **2.1. Remote-sensing data**

2 To investigate the impact of LAPs on snow albedo, we utilized the following MODIS  
3 data sets: surface albedo (MCD43C3;  $0.05^\circ \times 0.05^\circ$  resolution), snow cover  
4 (MYD10C1;  $0.05^\circ \times 0.05^\circ$  resolution), land cover type (MCD12C1;  $0.05^\circ \times 0.05^\circ$   
5 resolution), and atmospheric parameters (MYD08\_D3;  $1^\circ \times 1^\circ$  resolution). Each data  
6 set corresponds to January–February for the period 2003–2018  
7 (<https://earthdata.nasa.gov>, last access: 20 January 2019). MCD43C3 is the daily  
8 combined MODIS output derived from both the Terra and Aqua satellites, and provides  
9 black-sky albedo (directional hemispherical reflectance, DHF) and white-sky albedo  
10 (bi-hemispherical reflectance, BHF) at local solar noon for bands 1–7 (band 1, 620–670  
11 nm; band 2, 841–876 nm; band 3, 459–479 nm; band 4, 545–565 nm; band 5, 1230–  
12 1250 nm; band 6, 1628–1652 nm; band 7, 2105–2155 nm), as well as values for quality  
13 control, local noon solar zenith angle, and associated parameters. MCD43C3  
14 observations are weighted to estimate albedo on the 9th day of each 16-day period and  
15 have been corrected for the influence of local slope and aspect, atmospheric gases, and  
16 aerosols.

17 Snow-cover data are provided daily by MYD10C1 as a report of the snow-cover  
18 fraction (SCF), generated by the Normalized Difference Snow Index (NDSI).  
19 MCD12C1 provides a spatially aggregated and reprojected land-cover type, which is  
20 derived from the supervised classification of MODIS reflectance data, while MODIS  
21 MYD08\_D3 reports values of solar azimuth angle.



1 Average-daily solar radiation was obtained from NASA's Clouds and the Earth's  
2 Radiant Energy System (CERES: <https://ceres.larc.nasa.gov>, last access: 12 April 2019),  
3 part of the Earth Observing System comprising the Aqua, Terra, and S-NPP satellites.  
4 CERES provides instantaneous measurements of solar radiation, which are then  
5 converted to average-daily flux by angular dependence and empirical diurnal albedo  
6 modeling as the satellite passes through the point of descent (Doelling et al., 2013; Su  
7 et al., 2015; Loeb et al., 2018). We used the downward shortwave flux at the surface,  
8 provided by the "CERES Single Scanner Footprint 1.08 (SSF1deg)" product, to  
9 estimate average-daily RFLS under clear-sky conditions.

10 Shuttle Radar Topography Mission (SRTM) digital elevation data are provided by the  
11 US Geological Survey (<https://www.usgs.gov/>, last access: 9 December 2018) to adjust  
12 slope- and aspect-induced changes of surface solar radiation in complex terrain. The  
13 spatial resolution of SRTM data for the Northern Hemisphere is 30 m.

14

## 15 **2.2. Snow depth data**

16 Estimates of snow depth were obtained from the European Centre for Medium-Range  
17 Weather Forecasts (ECMWF) Interim Re-Analysis (ERA-Interim)  
18 (<https://www.ecmwf.int>, last access: 15 January 2019). ERA-Interim is a new  
19 generation of reanalysis based on a 12-hourly and 4-dimensional variational data  
20 assimilation (4D-Var) covering the period 1979–present. ERA-Interim performs better  
21 in model physics frameworks, data quality control, and background error criteria than





1 previous versions (Berrisford et al., 2011; Brun et al., 2013). In this study, we used  
2 snow-water equivalent (SWE) data for January–February covering the period 2003–  
3 2018. These data were generated by forecast models and updated according to a  
4 Cressman analysis of snow observations (Drusch et al., 2004; Dee et al., 2011). We note  
5 that the previous occurrence of false snow-free patches, arising from application of  
6 Cressman analysis in regions of sparse ground control, has been mitigated by ECMWF  
7 upgrades (Dee et al., 2011). Finally, SWE is converted to snow depth by assuming that  
8 average January–February snow density is  $\sim 200 \text{ kg m}^{-3}$ , consistent with snow-depth  
9 estimates by the Canadian Meteorological Centre (CMC) (Sturm et al., 1995; Brown  
10 and Mote, 2009).

11

### 12 **2.3. BC emission and deposition data**

13 We used the PKU-BC-2007 (EPKU: <http://inventory.pku.edu.cn>, last access: 5 June  
14 2019) global inventory, with a spatial resolution of  $0.1^\circ \times 0.1^\circ$ , to obtain BC emissions  
15 data for the period 2003–2014. PKU-BC-2007 was developed using a bottom-up  
16 method based on sub-national fuel-combustion data (Wang et al., 2013a, 2014b) and an  
17 updated set of BC emission factors (Wang et al., 2012). To constrain BC deposition  
18 fluxes during our study period, we applied the Modern-Era Retrospective Analysis for  
19 Research and Applications, version 2 (MERRA-2:  
20 <https://gmao.gsfc.nasa.gov/reanalysis/MERRA-2/>, last access: 5 June 2019), which  
21 simulates BC via a radiatively coupled version of the Goddard Chemistry, Aerosol,



1 Radiation, and Transport model (GOCART; Chin et al. 2002; Colarco et al. 2010). The  
2 efficacy of the GOCART aerosol module in simulating observable aerosol  
3 characteristics has been verified by a wealth of previous studies (e.g., Nowottnick et al.  
4 2010, 2011; Bian et al. 2013; Randles et al., 2017).

5

#### 6 **2.4. Climate model simulations**

7 We compared our remotely sensed retrievals of snow BC for the 2003–2014 study  
8 period with simulated concentrations derived from CMIP6 (<https://esgf-node.llnl.gov/>,  
9 last access: 15 July 2019), which coordinates the design and distribution of GCM  
10 simulations of past, present, and future climate. To date, only two CMIP participants,  
11 CESM2 and CESM2-WACCM, have provided simulations of snow BC concentrations.  
12 Therefore, we employed data derived from the CESM2 and CESM2-WACCM  
13 historical experiments, in conjunction with ERA-Interim SWE, MODIS-retrieved snow  
14 grain-size, and CERES downward shortwave flux data, to model RFLS for the study  
15 period. Simulations were performed using the Snow, Ice, and Aerosol Radiative  
16 (SNICAR) and Santa Barbara DISORT Atmospheric Radiative Transfer (SBDART)  
17 models, and modeled output compared to satellite-based retrievals. We also compared  
18 our retrieval-based estimates of RFLS to values simulated by the SNICAR model  
19 coupled with a GCM (Flanner et al., 2007, 2009).

20

#### 21 **3. Methods**



### 1 **3.1. Radiative transfer model**

2 In this study, we used the Santa Barbara DISORT Atmospheric Radiative Transfer  
3 (SBDART) model to calculate surface solar irradiance. Constituting one of the most  
4 widely applied models for calculating the atmospheric radiative transfer at Earth's  
5 surface, under both clear- and cloudy-sky conditions (Ricchiazzi et al., 1998), SBDART  
6 combines a low-resolution atmospheric transmission model, Discrete Ordinate  
7 Radiative Transfer (DISORT) module, and Mie scattering output for the scattering of  
8 light by ice crystals and water droplets (Stamnes et al., 1988; Fu et al., 2017). Radiative  
9 transfer equations for a vertically inhomogeneous, non-isothermal, plane-parallel  
10 atmosphere are integrated numerically using the DISORT module. SBDART comprises  
11 multiple standard atmospheric profiles, cloud models, basic surface types, standard  
12 types, as well as vertical distribution models for aerosols and gas absorption, and  
13 enables users to specify these input parameters in real values. In our study, we used  
14 SBDART to calculate the clear-sky spectral direct and diffuse solar radiation at local  
15 noon. Spectral radiation ranges from 0.3 to 1.3  $\mu\text{m}$ , at 0.01  $\mu\text{m}$  intervals, and with 1°  
16 latitude resolution. Average incident direct and diffuse solar spectra for January–  
17 February are shown in Fig. S1.

18 The Snow, Ice, and Aerosol Radiative (SNICAR) model is a two-stream multiple  
19 scattering radiative transfer model (Flanner et al., 2007, 2009) that has been used widely  
20 both to simulate the albedo, transmission, and vertical absorptivity of LAP-  
21 contaminated snowpack and to estimate RFLS (Painter et al., 2012a; Bryan et al., 2013;



1 Miller et al., 2016). SNICAR employs the theory proposed by Wiscombe and Warren  
2 (1980) and Toon et al. (1989). Specifically, snow is considered to be composed of  
3 aggregated ice spheres with optical effective radii ( $R_{eff}$ ) of 50–1500  $\mu\text{m}$  and lognormal  
4 distribution. SNICAR also accounts for incident radiation, surface spectral distribution,  
5 solar zenith angle, snow depth and density, snow layer number, and the type and  
6 concentration of LAPs in the snowpack. The model's ability to provide realistic  
7 simulations of snow albedo has been verified by several previous studies (Hadley and  
8 Kirchstetter, 2012; Meinander et al., 2013; Zhong et al., 2017; Wang et al., 2017).

9

### 10 **3.2. Retrieval of quantitative snow properties from remote sensing**

11 The variability of spectral snow albedo depends on the LAP content, grain size, and  
12 depth of the snowpack, in addition to solar zenith angle. As shown in Fig. 1a, the  
13 deposition of BC (as representative of LAPs generally) serves to decrease the albedo of  
14 snow significantly, particularly in the ultraviolet (UV) and VIS wavelengths, which  
15 account for approximately half of all direct solar irradiation and the majority of diffuse  
16 solar irradiation (Fig. S1). In contrast, the impact of BC on albedo is considerably  
17 smaller in NIR wavelengths and can be negligible at  $>\sim 1150$  nm. Snow depth plays a  
18 similar role to LAP content and primarily affects albedo in UV and VIS wavelengths  
19 (Fig. 1c).

20 Although snow albedo decreases with snow depth, previous studies have tended to  
21 assume a semi-infinite snowpack for which albedo is independent of depth. As a



1 consequence, the role of LAPs in albedo reduction has been overestimated for those  
2 areas where the snowpack is thin (Warren, 2013). In this study, we incorporated ERA-  
3 Interim SWE data in our SNICAR model simulations to correct for the snow-depth  
4 overestimation effect. In contrast, snow grain-size and solar zenith angle influence the  
5 snow albedo chiefly in NIR wavelengths (Fig. 1b, d). Specifically, albedo tends to  
6 decrease with increasing snow grain-size and declining solar zenith angle. In this study,  
7 we derived quantitative snow parameters (grain size, albedo reduction, and RFLS) from  
8 MODIS data in conjunction with the SNICAR and SBDART models. The specific  
9 workflow for retrieving RFLS from satellite data is shown in Fig. 2.

10

### 11 3.2.1. Retrieval of blue-sky albedo

12 The actual spectral albedo for a land surface at wavelength  $\lambda$  (also called blue-sky  
13 albedo:  $\alpha_{blue-sky,\lambda}$ ) can be calculated as follows:

$$14 \quad \alpha_{blue-sky,\lambda} = f_{dif,\lambda} \cdot \alpha_{white-sky,\lambda} + (1 - f_{dif,\lambda}) \cdot \alpha_{black-sky,\lambda} \quad (1)$$

15 where  $\alpha_{white-sky,\lambda}$  and  $\alpha_{black-sky,\lambda}$  are MODIS-derived values for white-sky and  
16 black-sky albedo, respectively, and  $f_{dif,\lambda}$  is the ratio of diffuse radiation to the total  
17 solar radiation flux (Lewis and Barnsley, 1994). The latter is calculated as follows:

$$18 \quad f_{dif,\lambda} = \frac{E_{dif}(\lambda; \varphi)}{E_{dif}(\lambda; \varphi) + E_{dir}(\lambda; \varphi)} \quad (2)$$

19 where  $\varphi$  is latitude, and  $E_{dif}(\lambda; \varphi)$  and  $E_{dir}(\lambda; \varphi)$  denote diffuse and direct  
20 spectral solar radiation, respectively, derived from the SBDART model.



1

### 2 3.2.2. Retrieval of snow cover and albedo values

3 As shown in Fig. 2, the snow-covered area is mapped according to the blue-sky albedo  
4 ( $\alpha_{blue-sky}$ ) in band 4 (band center  $\sim 555$  nm:  $\alpha_{blue-sky,\lambda}(\lambda_{VIS})$ ) and the Normalized  
5 Difference Snow Index (NDSI), both of which exceed 0.6 (Negi and Kokhanovsky,  
6 2011). NDSI is calculated as follows (Dozier and Marks, 1987; Hall et al., 1995):

$$7 \quad NDSI = \frac{\alpha_{blue-sky,\lambda}(\lambda_{VIS}) - \alpha_{blue-sky,\lambda}(\lambda_{SWIR})}{\alpha_{blue-sky,\lambda}(\lambda_{VIS}) + \alpha_{blue-sky,\lambda}(\lambda_{SWIR})} \quad (3)$$

8 where  $\alpha_{blue-sky,\lambda}(\lambda_{SWIR})$  is  $\alpha_{blue-sky,\lambda}$  in band 6 (band center  $\sim 1640$  nm).  
9 According to the MODIS Snow Products Collection 6 User Guide  
10 (<http://nsidc.org/data>), the Fractional Snow Cover ( $FSC$ ) can be calculated as follows:

$$11 \quad FSC = -0.01 + 1.45 \cdot NDSI \quad (4)$$

12 Accordingly, the identified snow-covered area (ISCA) has an  $FSC$  value of  $>86\%$  but  
13 not always 100%. Therefore, the MODIS-derived albedo for a particular ISCA is a  
14 combination of values representing both snow and the snow-free underlying surface.  
15 Following Pu et al. (2019), the snow albedo ( $\alpha_{snow,\lambda}^{MODIS}$ ) can be distinguished from the  
16 mixed albedo by the equation:

$$17 \quad \alpha_{blue-sky,\lambda} = \frac{E_{\lambda} \cdot FSC \cdot \alpha_{snow,\lambda}^{MODIS} + E_{\lambda} \cdot (1 - FSC) \cdot \alpha_{underlying,\lambda}}{E_{\lambda}}$$
$$18 \quad = FSC \cdot \alpha_{snow,\lambda}^{MODIS} + (1 - FSC) \cdot \alpha_{underlying,\lambda} \quad (5)$$

$$19 \quad \alpha_{snow,\lambda}^{MODIS} = \frac{\alpha_{blue-sky,\lambda} - (1 - FSC) \cdot \alpha_{underlying,\lambda}}{FSC} \quad (6)$$



1 where  $E_{\lambda}$  is total solar radiation.  $\alpha_{underlying,\lambda}$  represents the albedo of the  
2 underlying surface and was obtained from Siegmund and Menz (2005). As depicted in  
3 Fig. 3b, vegetation and bare soil are the main types of underlying surface in the ISCA.

4

### 5 **3.2.3. Retrieval of snow grain size**

6 The snow optical-equivalent grain size ( $R_{eff}$ ) is retrieved by fitting SNICAR-simulated  
7 snow albedo to MODIS-derived snow albedo at 1240 nm (the central wavelength of  
8 MODIS band 5), following the protocol of Nolin and Dozier (2000). This retrieval  
9 method is not influenced by liquid water and water vapor and has been employed  
10 widely in previous studies (e.g., Painter et al., 2013; Seidel et al., 2016). Both Nolin and  
11 Dozier (2000) and Pu et al. (2019) reported that the retrieved  $R_{eff}$  compares favorably  
12 with ground-based measurements of snow grain size. In this study, we chose to exclude  
13 the ISCA, where MODIS-derived snow albedo at 1240 nm is  $<0.3$ , to avoid  
14 misrepresenting  $R_{eff}$  (Tedesco et al., 2007).

15

### 16 **3.2.4. Retrieval of snow albedo reduction**

17 The instantaneous, spectrally integrated reduction in snow albedo due to LAPs  
18 ( $\Delta\alpha_{MODIS,ins}^{LAPs}$ ) is estimated for local-noon and clear-sky conditions, using solar radiation  
19 and the difference between MODIS-derived spectral snow albedo ( $\alpha_{snow,\lambda}^{MODIS}$ ) and  
20 simulated pure snow albedo ( $\alpha_{snow,\lambda}^{mdl}$ ). Because MODIS provides only four VIS bands,  
21 we fitted snow albedo data obtained via MODIS to a continuous 300–1300 nm spectrum



1 (with a 10 nm interval) following the method provided by Pu et al. (2019). Thereafter,  
2  $\Delta\alpha_{MODIS,ins}^{LAPs}$  can be calculated as follows:

$$3 \quad \Delta\alpha_{MODIS,ins}^{LAPs} = \frac{\sum_{\lambda=300nm}^{\lambda=1300nm} (\alpha_{snow,\lambda}^{mdl} - \alpha_{snow,\lambda}^{MODIS}) \cdot (E_{dir,\lambda} \cdot \cos\beta + E_{dif,\lambda}) \cdot \Delta\lambda}{\sum_{\lambda=300nm}^{\lambda=1300nm} (E_{dir,\lambda} \cdot \cos\beta + E_{dif,\lambda}) \cdot \Delta\lambda} \quad (7)$$

4 where  $\alpha_{snow,\lambda}^{mdl}$  is the pure snow albedo simulated by SNICAR using MODIS-derived  
5  $R_{eff}$  and ERA-Interim snow depth data,  $\alpha_{snow,\lambda}^{MODIS}$  is the continuous snow albedo  
6 derived from MODIS retrievals, and  $\Delta\lambda$  is 10 nm. Finally,  $\beta$  represents local solar  
7 zenith angle, which is obtained using the topographic correction method (Teillet et al.,  
8 1982; Negi and Kokhanovsky, 2011):

$$9 \quad \cos\beta = \cos\theta_0 \cos\theta_T + \sin\theta_0 \sin\theta_T \cos(\phi_0 - \phi_T) \quad (8)$$

10 for which  $\theta_0$  represents the solar zenith angle for a horizontal surface,  $\phi_0$  is the solar  
11 azimuth angle, and  $\theta_T$  and  $\phi_T$  denote slope inclination and aspect, respectively.  
12 Similarly, we used measurements of LAPs in contaminated snow to calculate the  
13 instantaneous, *in situ* reduction in snow albedo ( $\Delta\alpha_{in-situ,ins}^{LAPs}$ ). To derive a correction  
14 factor for MODIS retrievals, we applied a similar validation strategy to that of Zhu et  
15 al. (2017):

$$16 \quad c = \frac{1}{n} \sum_{i=1}^n \left( \frac{\Delta\alpha_{MODIS,ins}^{LAPs}}{\Delta\alpha_{in-situ,ins}^{LAPs}} \right) \quad (9)$$

17 where  $c$  is the correction factor for  $\Delta\alpha_{MODIS,ins}^{LAPs}$  and  $n$  is the number of the  
18 respective *in situ* measurements. Accordingly, the corrected albedo reduction  
19 ( $\Delta\alpha_{MODIS,corrected}^{LAPs}$ ) is calculated as follows:

$$20 \quad \Delta\alpha_{MODIS,corrected}^{LAPs} = \frac{1}{c} \cdot \Delta\alpha_{MODIS,ins}^{LAPs} \quad (10)$$





1

### 2 3.2.5. Retrieval of RFLS

3 The instantaneous, spectrally integrated RFLS ( $RF_{MODIS,ins}^{LAPs}$ ) is calculated for noon and  
4 clear-sky conditions as follows:

$$5 \quad RF_{MODIS,ins}^{LAPs} = \Delta\alpha_{MODIS,corrected}^{LAPs} \cdot \sum_{\lambda=300\text{ nm}}^{\lambda=1300\text{ nm}} (E_{dir,\lambda} \cdot \cos\beta + E_{dif,\lambda}) \cdot \Delta\lambda$$

6 (11)

7 We assumed that the properties for snow and LAPs remain invariable throughout the  
8 day and that the average-daily RFLS ( $RF_{MODIS,daily}^{LAPs}$ ) can be expressed as follows:

$$9 \quad RF_{MODIS,daily}^{LAPs} = \Delta\alpha_{MODIS,corrected}^{LAPs} \cdot (SW_{dir} \cdot \cos\beta + SW_{dif}) \quad (12)$$

10 where  $SW_{dir}$  and  $SW_{dif}$  represent the average-daily direct and diffuse downward  
11 shortwave fluxes, respectively, obtained from CERES under clear-sky conditions.

12

### 13 3.2.6. Attribution of spatial variability in snow albedo reductions and radiative 14 forcing

15 As demonstrated above, reductions in snow albedo and RFLS are dependent primarily  
16 on LAP content,  $R_{eff}$ , snow depth ( $SD$ ), solar zenith angle, surface topography, and  
17 solar radiation, the latter three of which can be categorized as the geographic factor ( $G$ ).

18 We used an impurity index ( $I_{LAPs}$ ) to represent the LAP content of the snowpack (Di  
19 Mauro et al., 2015; Pu et al., 2019), following the equation:

$$20 \quad I_{LAPs} = \frac{\ln(\alpha_{snow,band4}^{MODIS})}{\ln(\alpha_{snow,bands}^{MODIS})} \quad (13)$$



1 where  $\alpha_{snow,band4}^{MODIS}$  and  $\alpha_{snow,band5}^{MODIS}$  are the MODIS-derived snow albedo values for  
2 bands 4 and 5, respectively. We then calculated  $\Delta\alpha_{MODIS,corrected}^{LAPs}$  as follows:

$$3 \quad \Delta\alpha_{MODIS,corrected}^{LAPs} = f(I_{LAPs}, R_{eff}, SD, G) \quad (14)$$

4 Values for  $R_{eff}$ ,  $SD$ , and  $G$  were kept spatially constant as the averages  $\overline{R_{eff}}$ ,  $\overline{SD}$ ,  
5 and  $\overline{G}$ , with  $\overline{G}$  requiring spatially constant values for the solar zenith angle, surface  
6 topography, and solar radiation parameters. As a result, spatial variability in snow  
7 albedo reduction due to  $I_{LAPs}$  can be expressed as

$$8 \quad \Delta\alpha_{MODIS,corrected}^{LAPs}(I_{LAPs}) = f(I_{LAPs}, \overline{R_{eff}}, \overline{SD}, \overline{G}) \quad (15)$$

9 The following three equations were applied in a similar manner:

$$10 \quad \Delta\alpha_{MODIS,corrected}^{LAPs}(R_{eff}) = f(\overline{I_{LAPs}}, R_{eff}, \overline{SD}, \overline{G}) \quad (16)$$

$$11 \quad \Delta\alpha_{MODIS,corrected}^{LAPs}(SD) = f(\overline{I_{LAPs}}, \overline{R_{eff}}, SD, \overline{G}) \quad (17)$$

$$12 \quad \Delta\alpha_{MODIS,corrected}^{LAPs}(G) = f(\overline{I_{LAPs}}, \overline{R_{eff}}, \overline{SD}, G) \quad (18)$$

13 We then fitted  $\Delta\alpha_{MODIS,corrected}^{LAPs}$  through multiple linear regression:

$$14 \quad \Delta\alpha_{MODIS}^{LAPs,fit} = a \cdot \Delta\alpha_{MODIS,corrected}^{LAPs}(I_{LAPs}) + b \cdot$$
$$15 \quad \Delta\alpha_{MODIS,corrected}^{LAPs}(R_{eff}) + c \cdot \Delta\alpha_{MODIS,corrected}^{LAPs}(SD) + d \cdot \Delta\alpha_{MODIS,corrected}^{LAPs}(G)$$

16 (19)

17 where  $\Delta\alpha_{MODIS}^{LAPs,fit}$  is the fitted snow albedo reduction and a, b, c, and d denote the  
18 regression coefficients. Figure S3a illustrates how  $\Delta\alpha_{MODIS}^{LAPs,fit}$  can explain 98% of the  
19 variance in  $\Delta\alpha_{MODIS,corrected}^{LAPs}$ . Therefore, the attribution of spatial variance in



1  $\Delta\alpha_{MODIS,corrected}^{LAPs}$  can be replaced with  $\Delta\alpha_{MODIS}^{LAPs,fit}$ , enabling Eq. (19) to be written as  
 2 follows:

$$\begin{aligned}
 3 \quad \Delta\alpha_{MODIS}^{LAPs,fit} - \overline{\Delta\alpha_{MODIS}^{LAPs,fit}} &= a \cdot (\Delta\alpha_{MODIS,corrected}^{LAPs}(I_{LAPs}) - \\
 4 \quad \overline{\Delta\alpha_{MODIS,corrected}^{LAPs}(I_{LAPs})}) &+ b \cdot (\Delta\alpha_{MODIS,corrected}^{LAPs}(R_{eff}) - \\
 5 \quad \overline{\Delta\alpha_{MODIS,corrected}^{LAPs}(R_{eff})}) &+ c \cdot (\Delta\alpha_{MODIS,corrected}^{LAPs}(SD) - \\
 6 \quad \overline{\Delta\alpha_{MODIS,corrected}^{LAPs}(SD)}) &+ d \cdot (\Delta\alpha_{MODIS,corrected}^{LAPs}(G) - \overline{\Delta\alpha_{MODIS,corrected}^{LAPs}(G)}) \quad (20)
 \end{aligned}$$

7 and

$$\begin{aligned}
 8 \quad \Delta\alpha_{MODIS,anomaly}^{LAPs,fit} &= a \cdot \Delta\alpha_{MODIS,corrected,anomaly}^{LAPs}(I_{LAPs}) + b \cdot \\
 9 \quad \Delta\alpha_{MODIS,corrected,anomaly}^{LAPs}(R_{eff}) &+ c \cdot \Delta\alpha_{MODIS,corrected,anomaly}^{LAPs}(SD) + d \cdot \\
 10 \quad \Delta\alpha_{MODIS,corrected,anomaly}^{LAPs}(G). \quad (21)
 \end{aligned}$$

11 According to Huang and Yi (1991) and Pu et al. (2019), the fractional contribution of  
 12 LAP content to the variability in snow albedo reduction ( $R_{\Delta\alpha}^{LAPs}$ ) can be calculated as:

$$13 \quad R_{\Delta\alpha}^{LAPs} = \frac{1}{m} \sum_{j=1}^m \frac{(\alpha \cdot \Delta\alpha_{MODIS,corrected,anomaly}^{LAPs}(I_{LAPs})_j)^2}{K_j} \quad (22)$$

$$\begin{aligned}
 14 \quad K_j &= (a \cdot \Delta\alpha_{MODIS,corrected,anomaly}^{LAPs}(I_{LAPs})_j)^2 + (b \cdot \\
 15 \quad \Delta\alpha_{MODIS,corrected,anomaly}^{LAPs}(R_{eff})_j)^2 &+ (c \cdot \Delta\alpha_{MODIS,corrected,anomaly}^{LAPs}(SD)_j)^2 + \\
 16 \quad (d \cdot \Delta\alpha_{MODIS,corrected,anomaly}^{LAPs}(G)_j)^2 \quad (23)
 \end{aligned}$$

17 where  $m$  denotes the length of the data set. Values for  $R_{\Delta\alpha}^{R_{eff}}$ ,  $R_{\Delta\alpha}^{SD}$ , and  $R_{\Delta\alpha}^G$  can be  
 18 derived in the same way. Similarly, we can obtain the fractional contribution for  
 19 radiative forcing ( $R_{RF}^{LAPs}$ ,  $R_{RF}^{R_{eff}}$ ,  $R_{RF}^{SD}$ , and  $R_{RF}^G$ ).



1

## 2 **4. Results**

### 3 **4.1. Study area**

4 Figure 3a depicts the ISCA employed in this study. Most are located between 40°N and  
5 55°N in Eurasia and North America, and are dominated by grassland and bare-soil  
6 surfaces (Fig. 3b). Several mid–high-latitude regions that typically support a deep  
7 snowpack, including Russia, western Europe, and eastern North America, are not  
8 identified by MODIS as ISCA due to the broad distributions of forest and shrubland in  
9 those areas (Fig. 3b). This pattern is supported by Bond et al. (2006), who demonstrated  
10 that, under such vegetated conditions, LAPs in snow exert a relatively minor influence  
11 on radiative forcing. In the Arctic, where the polar night renders satellite-mounted  
12 sensors unable to detect radiation, only a small part of southern Greenland can be  
13 identified as snow-covered during January and February.

14 As illustrated in Fig. 3a, ISCA can be separated into four general regions according to  
15 geographical distribution and pollution conditions (Fig. 4a, b): northeastern China  
16 (NEC), Eurasia (EUA), North America (NA), and the Arctic. The following analysis of  
17 snow albedo reduction and RFLS concerns ISCA during the January–February study  
18 period.

19

### 20 **4.2. Global characteristics**



1 Previous studies have highlighted the dominant role of BC in light absorption by snow  
2 (Wang et al., 2013b; Dang et al., 2017). The spatial distribution of BC emissions density  
3 for the Northern Hemisphere in January–February is shown in Fig. 4a. Emissions  
4 density exhibits a strong spatial inhomogeneity, ranging from  $<10^{-1}$  to  $>10^4$  g km<sup>-2</sup>  
5 month<sup>-1</sup> over ISCA. The highest values occur in NEC, where the regional average of  
6 10750 g km<sup>-2</sup> month<sup>-1</sup> is considerably higher than values for EUA (5643 g km<sup>-2</sup>  
7 month<sup>-1</sup>) and NA (761 g km<sup>-2</sup> month<sup>-1</sup>), and the lowest values occur in the Arctic  
8 (average 76 g km<sup>-2</sup> month<sup>-1</sup>). The wet and dry deposition of BC constitute the primary  
9 mechanisms for BC accumulation in snow. As shown in Fig. 4b, the distribution of BC  
10 deposition (i.e., the sum of dry and wet deposition) is similar to BC emissions density,  
11 with the highest ( $3.26 \cdot 10^{-12}$  kg m<sup>-2</sup> s<sup>-1</sup>) and lowest ( $1.21 \cdot 10^{-13}$  kg m<sup>-2</sup> s<sup>-1</sup>) regional  
12 averages corresponding to NEC and the Arctic, respectively. Both NA and EUA return  
13 intermediate deposition values, with regional averages of  $5.75 \cdot 10^{-13}$  kg m<sup>-2</sup> s<sup>-1</sup> and  $1.78$   
14  $\cdot 10^{-12}$  kg m<sup>-2</sup> s<sup>-1</sup>, respectively. Together, these data indicate that the NEC snowpack is  
15 heavily polluted, and thus RFLS is likely to be highest, while the Arctic snowpack is  
16 the least contaminated.

17 In addition to LAP content, the physical properties of the snowpack, such as depth and  
18 grain size, also impact snow albedo (Fig. 1). As depicted in Fig. 4c, the average  
19 snowpack in NEC (0.19 m thick) is thinner than in both NA (0.26 m) and EUA (0.21  
20 m), implying a greater impact of snow depth on snow albedo and radiative forcing in  
21 NEC. The greatest snow depths occur in the Arctic ( $>1$  m) and can be considered semi-



1 infinite, meaning that the impact of depth on albedo and radiative forcing is negligible.  
2 Figure 4d shows the spatial distribution of MODIS-derived snow grain radius ( $R_{eff}$ ).  
3 In contrast to BC emissions density, BC deposition, and snow depth,  $R_{eff}$  exhibits  
4 minor spatial variability, with regional average values for NEC, EUA, NA, and the  
5 Arctic of 235  $\mu\text{m}$ , 227  $\mu\text{m}$ , 252  $\mu\text{m}$ , and 255  $\mu\text{m}$ , respectively. These values align with  
6 the findings of several previous studies (Painter et al., 2013; Seidel et al, 2016; Pu et  
7 al., 2019) and imply that the contribution of  $R_{eff}$  to spatial variability in snow albedo  
8 reduction and radiative forcing is negligible.

9 According to Eq. (10) and (11), local solar radiation is an important factor for  
10 determining RFLS. Figure 4e, f depicts the January–February averaged surface direct  
11 and diffuse solar irradiance, respectively, under clear-sky conditions. Average direct  
12 radiation values for EUA (138  $\text{W m}^{-2}$ ) and NA (147  $\text{W m}^{-2}$ ) are comparable to one  
13 another but high relative to NEC (87  $\text{W m}^{-2}$ ), which lies at a generally higher latitude  
14 ( $>40^\circ$ ). The lowest values occur in the Arctic (9  $\text{W m}^{-2}$ ) due to that region's extreme  
15 latitude. For diffuse radiation, average fluxes for NEC, EUA, NA, and the Arctic are 32  
16  $\text{W m}^{-2}$ , 46  $\text{W m}^{-2}$ , 36  $\text{W m}^{-2}$ , and 4  $\text{W m}^{-2}$ , respectively. In summary, these data indicate  
17 a smaller radiative forcing in the Arctic than in the other three regions.

18

### 19 4.3. Corrections based on *in situ* observations

20 *In situ* observations of snow albedo reduction ( $\Delta\alpha_{in-situ,ins}^{LAPs}$ ) were used to quantitatively  
21 correct MODIS retrievals through comparison with MODIS-retrieved snow albedo



1 reduction ( $\Delta\alpha_{MODIS,ins}^{LAPs}$ ). Figure S2 displays scatterplots of the ratios of  $\Delta\alpha_{MODIS,ins}^{LAPs}$  to  
2  $\Delta\alpha_{in-situ,ins}^{LAPs}$  ( $r_{in-situ}^{MODIS}$ ) for each sampling sites (Ye et al., 2012; Wang et al., 2013b,  
3 2017; Doherty et al., 2014). Briefly, for NA and EUA, where the snowpack is relatively  
4 pure, values for  $r_{in-situ}^{MODIS}$  mostly range between 1 and 12. In contrast, the heavily  
5 polluted snowpack in NEC returns  $r_{in-situ}^{MODIS}$  values ranging from 0.5 to 2.5, indicating  
6 a negative correlation between the biases of  $\Delta\alpha_{MODIS,ins}^{LAPs}$  and snow contamination, and  
7 thus supporting the findings of previous studies (Painter et al., 2012a; Pu et al., 2019).  
8 To improve the quality of MODIS retrievals, we developed the correction factors  
9  $c_{clean}$  for the relatively pure snowpack conditions observed in the EUA, NA, and the  
10 Arctic and  $c_{polluted}$  for the impure conditions found in NEC. According to Eq. (9),  
11 values for  $c_{clean}$  and  $c_{polluted}$  are 5.6 and 1.1, respectively. Hereafter, our analyses  
12 are based on the corrected MODIS retrievals.

13 Figure 5 compares the corrected MODIS retrievals to measurement-based results. For  
14 clean snow, the mean absolute error (MAE) of  $\Delta\alpha_{MODIS,corrected}^{LAPs}$  relative to  
15  $\Delta\alpha_{in-situ,ins}^{LAPs}$  is 0.0096, with a root mean square error (RMSE) of 0.0129,  
16 corresponding to respective radiative forcing MAE and RMSE values of  $3.0 \text{ W m}^{-2}$  and  
17  $3.8 \text{ W m}^{-2}$  for  $RF_{MODIS,ins}^{LAPs}$  and  $0.95 \text{ W m}^{-2}$  and  $1.2 \text{ W m}^{-2}$  for  $RF_{MODIS,daily}^{LAPs}$ . For  
18 polluted snow conditions, the MAE and RMSE are 0.0501 and 0.0622 for albedo  
19 reduction, respectively, with respective radiative forcing MAE and RMSE values of  $14$   
20  $\text{W m}^{-2}$  and  $18 \text{ W m}^{-2}$  for  $RF_{MODIS,ins}^{LAPs}$  and  $4.4 \text{ W m}^{-2}$  and  $5.5 \text{ W m}^{-2}$  for  $RF_{MODIS,daily}^{LAPs}$ .  
21 Together, these results imply that the corrected MODIS retrievals are plausible.



1 Nevertheless, we note that the correction used in this study is spatially rough due to the  
2 low density of *in situ* measurements, and that both the uncertainty and bias are non-  
3 negligible. As a result, we conducted a comprehensive series of comparisons between  
4 the MODIS-derived retrievals and values provided via surface measurements, model  
5 simulations, and remote sensing (see Sect. 5). We concluded that further field-based  
6 measurements of snow albedo are required to improve the quality of satellite retrievals.

7

#### 8 4.4. Spatial distributions of snow albedo reduction and radiative forcing

9 Figure 6 shows the spatial distributions and statistics of MODIS-based  
10  $\Delta\alpha_{MODIS,corrected}^{LAPs}$ ,  $RF_{MODIS,ins}^{LAPs}$ , and  $RF_{MODIS,daily}^{LAPs}$  retrievals. On average,  
11  $\Delta\alpha_{MODIS,corrected}^{LAPs}$ ,  $RF_{MODIS,ins}^{LAPs}$ , and  $RF_{MODIS,daily}^{LAPs}$  provide respective values of  
12 0.0246, 5.9 W m<sup>-2</sup>, and 1.7 W m<sup>-2</sup> for Northern Hemisphere ISCA. The highest  
13  $\Delta\alpha_{MODIS,corrected}^{LAPs}$  occurs in NEC, where the regional average of ~0.1669 exceeds those  
14 of EUA (~0.0210) and NA (~0.0181) by a factor of ~8–9. This feature reflects the  
15 relatively high rate of winter-time emissions over NEC, which results in the highest  
16 level of BC deposition over ISCA (Fig. 4a–b). In contrast, being located far from major  
17 sources of pollution, the relatively clean Arctic snowpack returns the lowest  
18  $\Delta\alpha_{MODIS,corrected}^{LAPs}$  (~0.0123) of the entire Northern Hemisphere.

19 Consistent with snow albedo reduction, the highest regional-average radiative forcing  
20 occurs in NEC, with respective  $RF_{MODIS,ins}^{LAPs}$  and  $RF_{MODIS,daily}^{LAPs}$  values of ~36 W m<sup>-2</sup>  
21 and ~11 W m<sup>-2</sup>, and the lowest regional average occurs in the Arctic, with  $RF_{MODIS,ins}^{LAPs}$





1 and  $RF_{MODIS,daily}^{LAPs}$  values of  $\sim 1.1 \text{ W m}^{-2}$  and  $\sim 0.29 \text{ W m}^{-2}$ , respectively. As well as  
2 receiving the lowest levels of pollution, the relatively low winter-time surface solar  
3 radiation also contributes to the Arctic returning the smallest radiative forcing (Fig. 4e–  
4 f). Regional-average radiative forcing for NA and EUA are both intermediate, with  
5  $RF_{MODIS,ins}^{LAPs}$  ( $RF_{MODIS,daily}^{LAPs}$ ) values of  $\sim 4.8 \text{ W m}^{-2}$  ( $\sim 1.4 \text{ W m}^{-2}$ ) and  $\sim 5.3 \text{ W m}^{-2}$  ( $\sim 1.5$   
6  $\text{W m}^{-2}$ ), respectively. Furthermore, because NA and EUA experience similar pollution  
7 conditions and are located at similar latitudes, both regions exhibit comparable radiative  
8 forcing.

9 On a regional level, NEC  $\Delta\alpha_{MODIS,corrected}^{LAPs}$  falls primarily within the range  $\sim 0.1177$ –  
10  $0.2157$ , and intra-regional variability is relatively small due to pervasive heavy  
11 pollution (Fig. 4). Compared to snow albedo reduction, the radiative forcing for NEC  
12 exhibits a slightly greater spatial variability due to latitude-dependent differences in the  
13 flux of surface solar radiation, with  $RF_{MODIS,ins}^{LAPs}$  ( $RF_{MODIS,daily}^{LAPs}$ ) ranging from  $\sim 24$   
14  $\text{W m}^{-2}$  to  $\sim 53 \text{ W m}^{-2}$  ( $\sim 6.9 \text{ W m}^{-2}$  to  $\sim 16 \text{ W m}^{-2}$ ). In NA, where the principal ISCA are  
15 located in southern Canada, the western US, and Central America Plains,  
16  $\Delta\alpha_{MODIS,corrected}^{LAPs}$  tends to range between  $\sim 0.0071$  and  $\sim 0.0309$ . The Central America  
17 Plains exhibit the highest value of  $\Delta\alpha_{MODIS,corrected}^{LAPs}$  ( $\sim 0.045$ ), with corresponding  
18  $RF_{MODIS,ins}^{LAPs}$  and  $RF_{MODIS,daily}^{LAPs}$  values of  $14 \text{ W m}^{-2}$  and  $\sim 3.9 \text{ W m}^{-2}$ , respectively. This  
19 region also displays a clear gradient in  $RF_{MODIS,ins}^{LAPs}$  ( $RF_{MODIS,daily}^{LAPs}$ ), with values  
20 increasing from  $< 5 \text{ W m}^{-2}$  ( $< 1 \text{ W m}^{-2}$ ) in the northwest to  $> 15 \text{ W m}^{-2}$  ( $> 4 \text{ W m}^{-2}$ ) in the  
21 southeast, in line with previously reported observational data (Doherty et al., 2014).



1 In EUA,  $\Delta\alpha_{MODIS,corrected}^{LAPs}$ ,  $RF_{MODIS,ins}^{LAPs}$ , and  $RF_{MODIS,daily}^{LAPs}$  fall largely within the  
2 respective ranges of  $\sim 0.0097\text{--}0.0352$ ,  $\sim 2.4\text{--}9.9\text{ W m}^{-2}$ , and  $\sim 0.69\text{--}2.9\text{ W m}^{-2}$ . The  
3 Middle East returns relatively high values for  $\Delta\alpha_{MODIS,corrected}^{LAPs}$  ( $>0.04$ ),  $RF_{MODIS,ins}^{LAPs}$   
4 ( $>12\text{ W m}^{-2}$ ), and  $RF_{MODIS,daily}^{LAPs}$  ( $>4\text{ W m}^{-2}$ ), likely due to the combined effects of  
5 elevated dust fluxes (Solomos et al., 2017) and high solar insolation at these low  
6 latitudes. Similar to the Middle East, northwestern China also exhibits relatively high  
7 values for  $\Delta\alpha_{MODIS,corrected}^{LAPs}$  ( $>0.035$ ),  $RF_{MODIS,ins}^{LAPs}$  ( $>11\text{ W m}^{-2}$ ), and  $RF_{MODIS,daily}^{LAPs}$   
8 ( $>3\text{ W m}^{-2}$ ), while this pattern likely reflects the influence of anthropogenic BC in  
9 addition to natural dust (Pu et al., 2017) (Fig. 4a–b). In contrast, Europe and Russia  
10 return the relatively low  $\Delta\alpha_{MODIS,corrected}^{LAPs}$  ( $<0.03$ ), with a  
11  $RF_{MODIS,ins}^{LAPs}$  ( $RF_{MODIS,daily}^{LAPs}$ ) value of  $<10\text{ W m}^{-2}$  ( $<3\text{ W m}^{-2}$ ), reflecting the generally  
12 low concentration of LAPs in this region. Finally, in the Arctic, where ISCA comprise  
13 only a small part of southern Greenland (see Sect. 4.1), respective  
14  $\Delta\alpha_{MODIS,corrected}^{LAPs}$ ,  $RF_{MODIS,ins}^{LAPs}$ , and  $RF_{MODIS,daily}^{LAPs}$  values fall within the ranges  
15  $\sim 0.0018\text{--}0.038$ ,  $\sim 0.18\text{--}3.8\text{ W m}^{-2}$ , and  $\sim 0.046\text{--}0.98\text{ W m}^{-2}$ .

16

#### 17 **4.5. Attribution to the spatial variability of snow albedo reduction and radiative** 18 **forcing**

19 Here, we address the attributions to the spatial variability of snow albedo reduction and  
20 radiative forcing. As discussed in Sect. 3.2.6, the spatial variability in snow albedo  
21 reduction and radiative forcing are largely dependent on LAP content, snow grain radius,



1 snow depth, and the geographic factor. Figure 7 illustrates the fractional contributions  
2 of each factor within the study regions. For the Northern Hemisphere as a whole, LAPs  
3 ( $I_{LAPs}$ ) is the greatest contributor (57.6%) to snow albedo reduction, followed by  $SD$   
4 (38.1%);  $R_{eff}$  and  $G$  have only a minor influence (2.7% and 1.6%, respectively) (Fig.  
5 7a). This result confirms that the concentration of LAPs in the snowpack plays a  
6 fundamental role in spatial variability of snow albedo reduction.

7 LAPs also constitute the dominant contributors to snow albedo reduction on a regional  
8 scale, accounting for 76.2% of the Arctic signal and 54.4% in EUA, and are the second  
9 largest contributor in both NEC (43.7%) and NA (48.1%). The contribution of  $SD$  is  
10 greatest in NEC (51.6%) and NA (49.8%), with slightly lower values in EUA (40.3%),  
11 reflecting the significant spatial variability in  $SD$  across these regions. In the Arctic,  
12 the snowpack is sufficiently thick to be considered a homogeneous, semi-infinite  
13 snowpack and thus the contribution of  $SD$  is negligible. In contrast,  $R_{eff}$  makes only  
14 minor contributions in NEC (3.9%), NA (1.4%), and EUA (3.3%) but is an important  
15 factor in the Arctic (22%). Finally,  $G$  makes the smallest contribution to snow albedo  
16 reduction (<2%), both on regional and global scales.

17 On a hemispheric scale, the greatest contributors to radiative forcing are LAP content  
18 (37.2%) and  $G$  (34.6%), followed by  $SD$  (27.9%). As with snow albedo reduction,  
19  $R_{eff}$  plays only a minor role (0.2%). Our data indicate that spatial variability in  
20 radiative forcing is highly dependent on  $G$ , a pattern that we attribute to the high degree  
21 of variability in latitude-dependent solar radiation among ISCA.



1 On a regional scale, the respective contributions of LAP content,  $G$ , and  $SD$  are also  
2 comparable among the four study areas, accounting for 27.4%, 37%, and 34% of  
3 radiative forcing in NEC, 24.9%, 38%, and 36.8% in NA, and 35.6%, 35.2%, and 27.2%  
4 in EUA. The Arctic radiative forcing is dominated by LAPs (52.8%) and  $G$  (46.4%).  
5 In summary, LAPs play a dominant role in the spatial variability of snow albedo  
6 reduction and radiative forcing. Our results also highlight the significant contribution  
7 of  $SD$  to snow albedo reduction and  $G$  to radiative forcing.

8

#### 9 **4.6. Comparisons with model simulations**

10 To investigate the global distribution and variance of RFLS, previous studies have  
11 tended to rely on Earth system models with minimal cross-checking from *in situ*  
12 measurements or remote sensing observations (Qian et al., 2015; Skiles et al., 2018). In  
13 this study, we compared MODIS retrievals with two model-based estimates to improve  
14 our understanding of the magnitude of RFLS on a global scale. Flanner et al. (2009)  
15 simulated springtime RFLS for the Northern Hemisphere by applying a Global Climate  
16 Model (GCM) coupled with a SNICAR model, the results of which are presented in  
17 Fig. 8a and Fig. S5a.

18 Figure 8b depicts the direct comparison of our MODIS retrievals ( $RF_{MODIS,daily}^{LAPs}$ ) to the  
19 simulations of Flanner et al. (2009) ( $RF_{GCM}$ ). In general,  $RF_{MODIS,daily}^{LAPs}$  and  $RF_{GCM}$   
20 are of the same magnitude and both fall in the range 0.10–4.6 W m<sup>-2</sup>. The MAE for



1  $RF_{GCM}$  against  $RF_{MODIS,daily}^{LAPs}$  is  $1.6 \text{ W m}^{-2}$ . Regionally, the average  $RF_{MODIS,daily}^{LAPs}$  in  
2 NEC (NA) is  $11 \text{ W m}^{-2}$  ( $1.4 \text{ W m}^{-2}$ ), a value that is higher by a factor of 2.5 (2.0) than  
3 the  $RF_{GCM}$  value of  $4.2 \text{ W m}^{-2}$  ( $0.69 \text{ W m}^{-2}$ ). In contrast,  $RF_{MODIS,daily}^{LAPs}$  ( $0.29 \text{ W m}^{-2}$ )  
4 for the Arctic is systematically lower than  $RF_{GCM}$  value ( $1.1 \text{ W m}^{-2}$ ) by a factor of 3.9.  
5 For EUA, average  $RF_{MODIS,daily}^{LAPs}$  ( $1.5 \text{ W m}^{-2}$ ) and  $RF_{GCM}$  ( $1.9 \text{ W m}^{-2}$ ) are comparable,  
6 while correlations between  $RF_{MODIS,daily}^{LAPs}$  and  $RF_{GCM}$  for NA, NEC, and the Arctic  
7 are all significant at the 99 % confidence level ( $R^2 = 0.36, 0.43, \text{ and } 0.72$ , respectively).

8 Employing ensemble-average snow BC concentrations from CESM2 and CESM2-  
9 WACCM, we also calculated January–February radiative forcing ( $RF_{CMIP6}$ ) for the  
10 Northern Hemisphere ISCA during the period 2003–2014 (Fig. 9a). Statistics are  
11 presented in Fig. S5b. Briefly,  $RF_{CMIP6}$  exhibits strong spatial inhomogeneity, with  
12 values ranging from  $0.068 \text{ W m}^{-2}$  to  $4.6 \text{ W m}^{-2}$ . The highest regional average in  
13  $RF_{CMIP6}$  occurs in NEC ( $\geq 5 \text{ W m}^{-2}$ ) and the lowest in the Arctic ( $\leq 0.2 \text{ W m}^{-2}$ ),  
14 consistent with  $RF_{MODIS,daily}^{LAPs}$ .

15 Figure 9b depicts the comparison of  $RF_{MODIS,daily}^{LAPs}$  and  $RF_{CMIP6}$ , for which the MAE  
16 of  $RF_{CMIP6}$  to  $RF_{MODIS,daily}^{LAPs}$  is  $0.90 \text{ W m}^{-2}$ . In NEC,  $RF_{CMIP6}$  ( $8.4 \text{ W m}^{-2}$ ) compares  
17 well with  $RF_{MODIS,daily}^{LAPs}$  ( $10.60 \text{ W m}^{-2}$ ), with a significant correlation at the 99%  
18 confidence level ( $R^2 = 0.43$ ). For NA and EUA,  $RF_{CMIP6}$  ( $0.69 \text{ W m}^{-2}$  and  $1.6 \text{ W m}^{-2}$ ,  
19 respectively) are lower than  $RF_{MODIS,daily}^{LAPs}$  ( $1.4 \text{ W m}^{-2}$  and  $1.5 \text{ W m}^{-2}$ , respectively)  
20 and the spatial correlations between them are poor. In the Arctic,  $RF_{CMIP6}$  is  
21 significantly correlated with  $RF_{MODIS,daily}^{LAPs}$  at the 99% confidence level ( $R^2 = 0.80$ ).



1 However,  $RF_{CMIP6}$  ( $0.15 \text{ W m}^{-2}$ ) is lower than  $RF_{MODIS,daily}^{LAPs}$  ( $0.29 \text{ W m}^{-2}$ ) by a factor  
2 of 2, an outcome that is contrary to the comparison between  $RF_{GCM}$  and  $RF_{MODIS,daily}^{LAPs}$ .  
3 Overall, the RFLS derived from our MODIS retrievals and modeling-based estimates  
4 exhibit a same magnitude over the Northern Hemisphere. In NEC, the MODIS- and  
5 model-derived estimates show good general agreement, indicating the satisfactory  
6 performance of Earth system modeling in this heavily polluted region. In NA and EUA,  
7 average radiative forcing values are comparable but the spatial correlation is relatively  
8 poor, while MODIS retrievals for the Arctic are significantly correlated with those  
9 simulations.

10

## 11 **5. Discussion**

12 In recent decades, there has been increasing scientific interest in snow LAPs due to  
13 their role in the climate system, and numerous studies have attempted to evaluate RFLS.  
14 In addition to making global-scale comparisons between our MODIS retrievals and  
15 model-based estimates, this study collects a comprehensive set of radiative forcing  
16 estimates, based on local-scale observations and remote sensing, to make quantitative  
17 regional- and global-scale comparisons and synthetically evaluate the magnitude of  
18 RFLS (Fig. 10). This approach also affords the opportunity to examine the MODIS  
19 retrievals used in our study.

20 For instantaneous RFLS, Pu et al. (2019) reported an average value for NEC of  $\sim 45$



1  $\text{W m}^{-2}$ , based on high-resolution (500 m) MODIS retrievals (Fig. 10a), which compares  
2 well with our findings ( $24\text{--}53 \text{ W m}^{-2}$ ). This agreement indicates that the coarse-  
3 resolution ( $0.05^\circ$ ) MODIS data used in this study are sufficient to establishing RFLS.  
4 In NA, Painter et al. (2012a) reported RFLS values of  $\sim 100\text{--}250 \text{ W m}^{-2}$  for the Upper  
5 Colorado River Basin, while Seidel et al. (2016) obtained values of  $20\text{--}200 \text{ W m}^{-2}$  in  
6 the Sierra Nevada and Rocky Mountain (Fig. 10a). For EUA, Di Mauro et al. (2015)  
7 estimated a maximum RFLS of  $153 \text{ W m}^{-2}$  in the European Alps (Fig. 10a). In the Arctic,  
8 Nagorski et al. (2019) reported a maximum RFLS for Alaska of  $>4 \text{ W m}^{-2}$  in May and  
9  $87 \text{ W m}^{-2}$  in June (Fig. 10a), while Ganey et al. (2017) provided a microbe-LAP-  
10 induced noontime radiative forcing of  $>\sim 20 \text{ W m}^{-2}$  (Fig. 10a). We note that the findings  
11 of previous studies are approximately one order of magnitude higher than our results in  
12 NA, EUA, and the Arctic. We attribute this partly to the fact that those earlier studies  
13 focused on a local-scale estimates for sites with high LAP loadings, whereas our study  
14 provides regional-scale estimates.

15 Relative to estimates of instantaneous RFLS, which are comparatively rare, average-  
16 daily RFLS has been paid more attention climatologically. Figure 10b shows the  
17 calculated average-daily RFLS based on *in situ* measurements and remote sensing.  
18 Dang et al. (2017) reported RFLS values of  $7\text{--}18 \text{ W m}^{-2}$ ,  $0.6\text{--}1.9 \text{ W m}^{-2}$ , and  $0.1\text{--}0.8$   
19  $\text{W m}^{-2}$  for northern China, North America, and the Arctic, respectively, which we note  
20 are comparable with our own retrievals. In NA, Sterle et al. (2013) estimated a daily-  
21 averaged RFLS of  $\sim 5 \text{ W m}^{-2}$  for the eastern Sierra Nevada, while Miller et al. (2016)



1 reported a daily RFLS of  $<4 \text{ W m}^{-2}$  in the San Juan Mountains. Both values are higher  
2 than our estimate ( $\sim 1.4 \text{ W m}^{-2}$ ), potentially due to the significant dust deposition in  
3 those areas.

4 Figure 10c shows the average-daily RFLS simulated by regional and/or global climate  
5 models. For NEC, Zhao et al. (2014) and Qian et al. (2014) reported values of 10  
6  $\text{W m}^{-2}$  and  $5\text{--}10 \text{ W m}^{-2}$ , respectively. In NA, the latter study also provided an estimate  
7 of  $2\text{--}7 \text{ W m}^{-2}$  for the central Rockies and southern Alberta (Qian et al., 2014), while  
8 Oaida et al. (2015) reported an average RFLS of  $16 \text{ W m}^{-2}$  over the western US. In  
9 EUA, Flanner et al. (2014) concluded that a RFLS of  $0.1\text{--}1 \text{ W m}^{-2}$  was caused by the  
10 deposition of volcanic ash in snow. Finally, Qian et al. (2014) and Qi et al. (2017)  
11 estimated RFLS values of  $<0.3 \text{ W m}^{-2}$  and  $0.024\text{--}0.39 \text{ W m}^{-2}$  for the Arctic, respectively.

12 We consider our retrievals for NEC, EUA, and the Arctic to be comparable with these  
13 regional model simulations, despite some disparity. However, we note that our result  
14 for NA is significantly lower than those of previous studies.

15 For the North Hemisphere as a whole, Bond et al. (2013) estimated a climate forcing of  
16  $0.13 \text{ W m}^{-2}$ , while Hansen and Nazarenko (2004) and Wang et al. (2014a) reported  
17 RFLS values of  $0.3 \text{ W m}^{-2}$  and  $0.45 \text{ W m}^{-2}$ , respectively. Each of these previous values  
18 is significantly lower than our retrieval ( $\sim 1.7 \text{ W m}^{-2}$ ). We attribute this disparity to the  
19 inclusion in those studies of low-LAP boreal forests, which contribute very little to  
20 overall radiative forcing yet exhibit a high degree of uncertainty. Skiles et al. (2018)  
21 also concluded that modeled RFLS might be biased if the snow-covered area itself is





1 not accurately represented.

2 Overall, we consider our MODIS-based retrievals to be physical realistic on both  
3 regional and global scales, although we note a number of differences between our  
4 results and those generated by different methods. On the other hand, while *in situ*  
5 measurements are the most precise, their spatial coverage is restricted by logistical  
6 limitations and the extreme environments involved. Conversely, models can provide  
7 broad perspectives of climatic impacts yet are typically undermined by large uncertainty.  
8 Therefore, we argue that remote sensing provides a powerful technique, with high  
9 spatial and temporal resolutions, that can bridge the gap between *in situ* measurements  
10 and climate models and reduce the uncertainties associated with the latter. Further  
11 retrieval of remote-sensing data, including the use of multiple satellites and sensors, is  
12 therefore warranted to exploit this opportunity fully. We also indicate the fact that parts  
13 of central EUA, such as Middle East, are characterized by high dust deposition,  
14 however, studies are barely performed but desired. Finally, we note that *in situ*  
15 observations remain limited, and more field campaigns are needed to constrain remote  
16 sensing retrievals and modeling simulations.

17

## 18 **6. Conclusion**

19 We presented a global-scale evaluation of the radiative forcing of LAPs in the Northern  
20 Hemisphere snowpack (RFLS), estimated from remote-sensing data. The satellite-  
21 retrieved RFLS also has implications for expanding the value of limited *in situ*



1 measurements, which can provide valuable information for climate models and help  
2 optimize model simulations.

3 Based on the corrected snow albedo reduction ( $\Delta\alpha_{MODIS,corrected}^{LAPs}$ ), we used the  
4 SBDART model to calculate instantaneous RFLS ( $RF_{MODIS,ins}^{LAPs}$ ) and average-daily  
5 RFLS ( $RF_{MODIS,daily}^{LAPs}$ ) during January–February for the period 2003–2018. For the  
6 Northern Hemisphere as a whole, average  $\Delta\alpha_{MODIS,corrected}^{LAPs}$  is  $\sim 0.0246$ ,  $RF_{MODIS,ins}^{LAPs}$   
7 is  $\sim 5.9 \text{ W m}^{-2}$ , and  $RF_{MODIS,daily}^{LAPs}$  is  $\sim 1.7 \text{ W m}^{-2}$ . We also observed distinct spatial  
8 variability in snow albedo reduction and RFLS. The highest regional-average  
9  $\Delta\alpha_{MODIS,corrected}^{LAPs}$  ( $\sim 0.1669$ ),  $RF_{MODIS,daily}^{LAPs}$  ( $\sim 11 \text{ W m}^{-2}$ ), and  $RF_{MODIS,ins}^{LAPs}$  ( $\sim 36$   
10  $\text{ W m}^{-2}$ ) occur in northeastern China, while the lowest regional averages of  $\sim 0.0123$ ,  
11  $\sim 0.29 \text{ W m}^{-2}$ , and  $\sim 1.1 \text{ W m}^{-2}$ , respectively, are observed in the Arctic.

12 Following this assessment, we made quantitative attributions of the spatial variability  
13 in snow albedo reduction and radiative forcing. Our results indicate that the LAP  
14 content is the largest contributor (57.6%) to spatial variance in snow albedo reduction,  
15 followed by snow depth (38.1%), whereas snow grain size (2.7%) and the geographic  
16 factor  $G$  (1.6%) are only minor contributors on a Northern Hemispheric scale. LAP  
17 content and  $G$  account for 37.2% and 34.6% of the spatial variability of radiative  
18 forcing, respectively, following by  $SD$  (27.9%) over Northern Hemisphere.

19 Retrieved RFLS values are compared spatially with the model-derived estimates of the  
20 Global Climate Model (GCM) and the Coupled Model Intercomparison Project (CMIP  
21 Phase 6). Our results indicate that MODIS retrievals provide show the same magnitude



1 with modeled estimates for Northern Hemisphere. However, although the Earth system  
2 models perform well in NEC, there remain large uncertainties in the Arctic. To evaluate  
3 and examine the MODIS retrievals synthetically, we then compared the retrieved RFLS  
4 to previously published estimates, including local-scale observations, remote sensing  
5 retrievals, and regional- and global-scale model simulations. The results of this  
6 evaluation suggest that MODIS retrievals are generally realistic, despite a number of  
7 important differences among the various methods.

8 Finally, we urge the community to expand the ground-based measurements of the global  
9 snowpack, particularly in those regions currently lacking *in situ* observations. Such  
10 development would help further constrain and improve satellite-based retrievals in the  
11 future. We propose that climate models incorporating these refined remote sensing  
12 retrievals should be able to capture the RFLS more accurately, thereby providing more  
13 reliable estimates of the future impacts of global climate change.

14

15 **Data availability.**

16 MODIS data can be found at <https://earthdata.nasa.gov/> (last access: 20 January 2019).  
17 CERES data can be found from NASA's Clouds and the Earth's Radiant Energy System  
18 at <https://ceres.larc.nasa.gov> (last access: 12 April 2019). Shuttle Radar Topography  
19 Mission (SRTM) digital elevation data are provided by the US Geological Survey at  
20 <https://www.usgs.gov/> (last access: 9 December 2018). Snow depth can be found from  
21 ERA-Interim at <https://www.ecmwf.int> (last access: 15 January 2019). BC emission



1 data can be found at <http://inventory.pku.edu.cn> (last access: 5 June 2019). BC  
2 deposition data can be found at <https://gmao.gsfc.nasa.gov/reanalysis/MERRA-2/> (last  
3 access: 5 June 2019). CMIP6 data can be found at <https://esgf-node.llnl.gov/> (last access:  
4 15 July 2019). Surface measurement datasets are from Wang et al. (2013, 2017), Ye et  
5 al. (2012) and Doherty et al. (2010, 2014). Springtime radiative forcing due to LAPs in  
6 snow is derived from a GCM run by Flanner et al. (2007).

#### 7 **Author contributions.**

8 PW and WX designed the study and evolved the overarching research goals and aims.  
9 CJC carried the study out and wrote the first draft with contributions from all co-authors.  
10 CJC and STL applied formal techniques such as statistical, mathematical and  
11 computational to analyze study data. ZY prepared input data and managed activities to  
12 annotate, scrub data and maintain research data. WDY completed the implementation  
13 of the computer code and supporting algorithms used for the calculations in this study.  
14 PW and WX assumed oversight and leadership responsibility for the research activity  
15 planning and execution. All authors contributed to the improvement of results and  
16 revised the final paper.

#### 17 **Competing interests.**

18 The authors declare that they have no conflict of interest.

#### 19 **Acknowledgments**

20 This research was supported jointly by the National Key R&D Program of China  
21 (2019YFA0606800), the National Natural Science Foundation of China (grants



1 41975157, 41775144, and 41875091).

2

### 3 **References**

4 Bair, E. H., Rittger, K., Skiles, S. M., and Dozier, J.: An Examination of Snow Albedo  
5 Estimates From MODIS and Their Impact on Snow Water Equivalent Reconstruction,  
6 *Water Resources Research*, 10.1029/2019wr024810, 2019.

7 Barnett, T. P., Adam, J. C., and Lettenmaier, D. P.: Potential impacts of a warming  
8 climate on water availability in snow-dominated regions, *Nature*, 438, 303-309,  
9 10.1038/nature04141, 2005.

10 Berrisford, P., Kållberg, P., Kobayashi, S., Dee, D., Uppala, S., Simmons, A. J., Poli, P.,  
11 and Sato, H.: Atmospheric conservation properties in ERA-Interim, *Quarterly Journal*  
12 *of the Royal Meteorological Society*, 137, 1381-1399, 10.1002/qj.864, 2011.

13 Bian, H., Colarco, P. R., Chin, M., Chen, G., Rodriguez, J. M., Liang, Q., Blake, D.,  
14 Chu, D. A., da Silva, A., Darmenov, A. S., Diskin, G., Fuelberg, H. E., Huey, G., Kondo,  
15 Y., Nielsen, J. E., Pan, X., and Wisthaler, A.: Source attributions of pollution to the  
16 Western Arctic during the NASA ARCTAS field campaign, *Atmospheric Chemistry*  
17 *and Physics*, 13, 4707-4721, 10.5194/acp-13-4707-2013, 2013.

18 Bond, T. C., Habib, G., and Bergstrom, R. W.: Limitations in the enhancement of visible  
19 light absorption due to mixing state, *Journal of Geophysical Research*, 111,  
20 10.1029/2006jd007315, 2006.



- 1 Bond, T. C., Doherty, S. J., Fahey, D. W., Forster, P. M., Berntsen, T., DeAngelo, B. J.,  
2 Flanner, M. G., Ghan, S., Kärcher, B., Koch, D., Kinne, S., Kondo, Y., Quinn, P. K.,  
3 Sarofim, M. C., Schultz, M. G., Schulz, M., Venkataraman, C., Zhang, H., Zhang, S.,  
4 Bellouin, N., Guttikunda, S. K., Hopke, P. K., Jacobson, M. Z., Kaiser, J. W., Klimont,  
5 Z., Lohmann, U., Schwarz, J. P., Shindell, D., Storelvmo, T., Warren, S. G., and Zender,  
6 C. S.: Bounding the role of black carbon in the climate system: A scientific assessment,  
7 *Journal of Geophysical Research: Atmospheres*, 118, 5380-5552, 10.1002/jgrd.50171,  
8 2013.
- 9 Brandt, R. E., Warren, S. G., and Clarke, A. D.: A controlled snowmaking experiment  
10 testing the relation between black carbon content and reduction of snow albedo, *Journal*  
11 *of Geophysical Research*, 116, 10.1029/2010jd015330, 2011.
- 12 Brown, R. D., and Mote, P. W.: The Response of Northern Hemisphere Snow Cover to  
13 a Changing Climate, *Journal of Climate*, 22, 2124-2145, 10.1175/2008jcli2665.1, 2009.
- 14 Brun, E., Vionnet, V., Boone, A., Decharme, B., Peings, Y., Valette, R., Karbou, F., and  
15 Morin, S.: Simulation of Northern Eurasian Local Snow Depth, Mass, and Density  
16 Using a Detailed Snowpack Model and Meteorological Reanalyses, *Journal of*  
17 *Hydrometeorology*, 14, 203-219, 10.1175/jhm-d-12-012.1, 2013.
- 18 Bryant, A. C., Painter, T. H., Deems, J. S., and Bender, S. M.: Impact of dust radiative  
19 forcing in snow on accuracy of operational runoff prediction in the Upper Colorado  
20 River Basin, *Geophysical Research Letters*, 40, 3945-3949, 10.1002/grl.50773, 2013.



- 1 Chin, M., Ginoux, P., Kinne, S., Torres, O., Holben, B. N., Duncan, B. N., Martin, R.  
2 V., Logan, J. A., Higurashi, A., and Nakajima, T.: Tropospheric Aerosol Optical  
3 Thickness from the GOCART Model and Comparisons with Satellite and Sun  
4 Photometer Measurements, *Journal of the Atmospheric Sciences*, 59, 461-483,  
5 10.1175/1520-0469(2002)059<0461:taotfi>2.0.co;2, 2002.
- 6 Colarco, P., da Silva, A., Chin, M., and Diehl, T.: Online simulations of global aerosol  
7 distributions in the NASA GEOS-4 model and comparisons to satellite and ground-  
8 based aerosol optical depth, *Journal of Geophysical Research*, 115,  
9 10.1029/2009jd012820, 2010.
- 10 Colombo, R., Garzonio, R., Di Mauro, B., Dumont, M., Tuzet, F., Cogliati, S., Pozzi,  
11 G., Maltese, A., and Cremonese, E.: Introducing Thermal Inertia for Monitoring  
12 Snowmelt Processes With Remote Sensing, *Geophysical Research Letters*, 46, 4308-  
13 4319, 10.1029/2019gl082193, 2019.
- 14 Dang, C., Brandt, R. E., and Warren, S. G.: Parameterizations for narrowband and  
15 broadband albedo of pure snow and snow containing mineral dust and black carbon,  
16 *Journal of Geophysical Research: Atmospheres*, 120, 5446-5468,  
17 10.1002/2014jd022646, 2015.
- 18 Dang, C., Warren, S. G., Fu, Q., Doherty, S. J., Sturm, M., and Su, J.: Measurements of  
19 light-absorbing particles in snow across the Arctic, North America, and China: Effects  
20 on surface albedo, *J Geophys Res-Atmos*, 122, 10149-10168, 2017.



- 1 Dee, D. P., Uppala, S. M., Simmons, A. J., Berrisford, P., Poli, P., Kobayashi, S., Andrae,  
2 U., Balmaseda, M. A., Balsamo, G., Bauer, P., Bechtold, P., Beljaars, A. C. M., van de  
3 Berg, L., Bidlot, J., Bormann, N., Delsol, C., Dragani, R., Fuentes, M., Geer, A. J.,  
4 Haimberger, L., Healy, S. B., Hersbach, H., Hólm, E. V., Isaksen, L., Kållberg, P.,  
5 Köhler, M., Matricardi, M., McNally, A. P., Monge-Sanz, B. M., Morcrette, J. J., Park,  
6 B. K., Peubey, C., de Rosnay, P., Tavolato, C., Thépaut, J. N., and Vitart, F.: The ERA-  
7 Interim reanalysis: configuration and performance of the data assimilation system,  
8 Quarterly Journal of the Royal Meteorological Society, 137, 553-597, 10.1002/qj.828,  
9 2011.
- 10 Deems, J. S., Painter, T. H., Barsugli, J. J., Belnap, J., and Udall, B.: Combined impacts  
11 of current and future dust deposition and regional warming on Colorado River Basin  
12 snow dynamics and hydrology, Hydrology and Earth System Sciences, 17, 4401-4413,  
13 10.5194/hess-17-4401-2013, 2013.
- 14 Di Mauro, B., Fava, F., Ferrero, L., Garzonio, R., Baccolo, G., Delmonte, B., and  
15 Colombo, R.: Mineral dust impact on snow radiative properties in the European Alps  
16 combining ground, UAV, and satellite observations, Journal of Geophysical Research:  
17 Atmospheres, 120, 6080-6097, 10.1002/2015jd023287, 2015.
- 18 Di Mauro, B., Baccolo, G., Garzonio, R., Giardino, C., Massabò, D., Piazzalunga, A.,  
19 Rossini, M., and Colombo, R.: Impact of impurities and cryoconite on the optical  
20 properties of the Morteratsch Glacier (Swiss Alps), The Cryosphere, 11, 2393-2409,  
21 10.5194/tc-11-2393-2017, 2017.





- 1 Di Mauro, B., Garzonio, R., Rossini, M., Filippa, G., Pogliotti, P., Galvagno, M., Morra
- 2 di Cella, U., Migliavacca, M., Baccolo, G., Clemenza, M., Delmonte, B., Maggi, V.,
- 3 Dumont, M., Tuzet, F., Lafaysse, M., Morin, S., Cremonese, E., and Colombo, R.:
- 4 Saharan dust events in the European Alps: role in snowmelt and geochemical
- 5 characterization, *The Cryosphere*, 13, 1147-1165, 10.5194/tc-13-1147-2019, 2019.
- 6 Doelling, D. R., Loeb, N. G., Keyes, D. F., Nordeen, M. L., Morstad, D., Nguyen, C.,
- 7 Wielicki, B. A., Young, D. F., and Sun, M.: Geostationary Enhanced Temporal
- 8 Interpolation for CERES Flux Products, *Journal of Atmospheric and Oceanic*
- 9 *Technology*, 30, 1072-1090, 10.1175/jtech-d-12-00136.1, 2013.
- 10 Doherty, S. J., Warren, S. G., Grenfell, T. C., Clarke, A. D., and Brandt, R. E.: Light-
- 11 absorbing impurities in Arctic snow, *Atmospheric Chemistry and Physics*, 10, 11647-
- 12 11680, 10.5194/acp-10-11647-2010, 2010.
- 13 Doherty, S. J., Dang, C., Hegg, D. A., Zhang, R., and Warren, S. G.: Black carbon and
- 14 other light-absorbing particles in snow of central North America, *Journal of*
- 15 *Geophysical Research: Atmospheres*, 119, 12,807-812,831, 10.1002/2014jd022350,
- 16 2014.
- 17 Dozier, J., and Marks, D.: Snow Mapping and Classification from Landsat Thematic
- 18 Mapper Data, *Annals of Glaciology*, 9, 97-103,
- 19 <https://doi.org/10.3189/S026030550000046X>, 1987.
- 20 Drusch, M., Vasiljevic, D., and Viterbo, P.: ECMWF's Global Snow Analysis:



- 1 Assessment and Revision Based on Satellite Observations, Journal of Applied  
2 Meteorology, 43, 1282-1294, 10.1175/1520-0450(2004)043<1282:egsaaa>2.0.co;2,  
3 2004.
- 4 Eyring, V., Bony, S., Meehl, G. A., Senior, C. A., Stevens, B., Stouffer, R. J., and Taylor,  
5 K. E.: Overview of the Coupled Model Intercomparison Project Phase 6 (CMIP6)  
6 experimental design and organization, Geosci Model Dev, 9, 1937-1958, 10.5194/gmd-  
7 9-1937-2016, 2016.
- 8 Flanner, M. G., Zender, C. S., Randerson, J. T., and Rasch, P. J.: Present-day climate  
9 forcing and response from black carbon in snow, Journal of Geophysical Research, 112,  
10 10.1029/2006jd008003, 2007.
- 11 Flanner, M. G., Zender, C. S., Hess, P. G., Mahowald, N. M., Painter, T. H., Ramanathan,  
12 V., and Rasch, P. J.: Springtime warming and reduced snow cover from carbonaceous  
13 particles, Atmospheric Chemistry and Physics, 9, 2481-2497, 10.5194/acp-9-2481-  
14 2009, 2009.
- 15 Flanner, M. G., Shell, K. M., Barlage, M., Perovich, D. K., and Tschudi, M. A.:  
16 Radiative forcing and albedo feedback from the Northern Hemisphere cryosphere  
17 between 1979 and 2008, Nature Geoscience, 4, 151-155, 10.1038/ngeo1062, 2011.
- 18 Flanner, M. G., Gardner, A. S., Eckhardt, S., Stohl, A., and Perket, J.: Aerosol radiative  
19 forcing from the 2010 Eyjafjallajökull volcanic eruptions, Journal of Geophysical  
20 Research: Atmospheres, 119, 9481-9491, 10.1002/2014jd021977, 2014.



- 1 Fu, Y., Zhu, J., Yang, Y., Yuan, R., Liu, G., Xian, T., and Liu, P.: Grid-cell aerosol direct
- 2 shortwave radiative forcing calculated using the SBDART model with MODIS and
- 3 AERONET observations: An application in winter and summer in eastern China,
- 4 *Advances in Atmospheric Sciences*, 34, 952-964, 10.1007/s00376-017-6226-z, 2017.
- 5 Ganey, G. Q., Loso, M. G., Burgess, A. B., and Dial, R. J.: The role of microbes in
- 6 snowmelt and radiative forcing on an Alaskan icefield, *Nature Geoscience*, 10, 754-759,
- 7 10.1038/ngeo3027, 2017.
- 8 Grell, G. A., Peckham, S. E., Schmitz, R., McKeen, S. A., Frost, G., Skamarock, W. C.,
- 9 and Eder, B.: Fully coupled “online” chemistry within the WRF model, *Atmospheric*
- 10 *Environment*, 39, 6957-6975, 10.1016/j.atmosenv.2005.04.027, 2005.
- 11 Hadley, O. L., and Kirchstetter, T. W.: Black-carbon reduction of snow albedo, *Nature*
- 12 *Climate Change*, 2, 437-440, 10.1038/nclimate1433, 2012.
- 13 Hall, A., and Qu, X.: Using the current seasonal cycle to constrain snow albedo
- 14 feedback in future climate change, *Geophysical Research Letters*, 33,
- 15 10.1029/2005gl025127, 2006.
- 16 Hall, D. K., Riggs, G. A., and Salomonson, V. V.: Development of methods for mapping
- 17 global snow cover using moderate resolution imaging spectroradiometer data, *Remote*
- 18 *Sensing of Environment*, 54, 127-140, 10.1016/0034-4257(95)00137-p, 1995.
- 19 Hansen, J., and Nazarenko, L.: Soot climate forcing via snow and ice albedos, *P Natl*
- 20 *Acad Sci USA*, 101, 423-428, 2004.



- 1 Huang, J. P. and Yi, Y. H.: Inversion of a nonlinear dynamic-model from the observation,
- 2 *Sci. China Chem.*, 34, 1246–1246, 1991.
- 3 Huang, J., Fu, Q., Zhang, W., Wang, X., Zhang, R., Ye, H., and Warren, S. G.: Dust and
- 4 Black Carbon in Seasonal Snow Across Northern China, *Bulletin of the American*
- 5 *Meteorological Society*, 92, 175-181, 10.1175/2010bams3064.1, 2011.
- 6 Kaspari, S., Painter, T. H., Gysel, M., Skiles, S. M., and Schwikowski, M.: Seasonal
- 7 and elevational variations of black carbon and dust in snow and ice in the Solu-Khumbu,
- 8 Nepal and estimated radiative forcings, *Atmospheric Chemistry and Physics*, 14, 8089-
- 9 8103, 10.5194/acp-14-8089-2014, 2014.
- 10 Kaspari, S., McKenzie Skiles, S., Delaney, I., Dixon, D., and Painter, T. H.: Accelerated
- 11 glacier melt on Snow Dome, Mount Olympus, Washington, USA, due to deposition of
- 12 black carbon and mineral dust from wildfire, *Journal of Geophysical Research:*
- 13 *Atmospheres*, 120, 2793-2807, 10.1002/2014jd022676, 2015.
- 14 Lee, L. A., Reddington, C. L., and Carslaw, K. S.: On the relationship between aerosol
- 15 model uncertainty and radiative forcing uncertainty, *Proc Natl Acad Sci U S A*, 113,
- 16 5820-5827, 10.1073/pnas.1507050113, 2016.
- 17 Lewis, P., and Barnsley, M.: Influence of the sky radiance distribution on various
- 18 formulations of the earth surface albedo, 6th International Symposium on Physical
- 19 Measurements and Signatures in Remote Sensing, ISPRS, 1994, 707-715,
- 20 Liou, K. N., Takano, Y., He, C., Yang, P., Leung, L. R., Gu, Y., and Lee, W. L.:



- 1 Stochastic parameterization for light absorption by internally mixed BC/dust in snow
- 2 grains for application to climate models, *Journal of Geophysical Research:*
- 3 *Atmospheres*, 119, 7616-7632, 10.1002/2014jd021665, 2014.
- 4 Loeb, N. G., Doelling, D. R., Wang, H., Su, W., Nguyen, C., Corbett, J. G., Liang, L.,
- 5 Mitrescu, C., Rose, F. G., and Kato, S.: Clouds and the Earth's Radiant Energy System
- 6 (CERES) Energy Balanced and Filled (EBAF) Top-of-Atmosphere (TOA) Edition-4.0
- 7 Data Product, *Journal of Climate*, 31, 895-918, 10.1175/jcli-d-17-0208.1, 2018.
- 8 Meinander, O., Kazadzis, S., Arola, A., Riihelä, A., Räisänen, P., Kivi, R., Kontu, A.,
- 9 Kouznetsov, R., Sofiev, M., Svensson, J., Suokanerva, H., Aaltonen, V., Manninen, T.,
- 10 Roujean, J. L., and Hautecoeur, O.: Spectral albedo of seasonal snow during intensive
- 11 melt period at Sodankylä, beyond the Arctic Circle, *Atmospheric Chemistry and*
- 12 *Physics*, 13, 3793-3810, 10.5194/acp-13-3793-2013, 2013.
- 13 Miller, S. D., Wang, F., Burgess, A. B., Skiles, S. M., Rogers, M., and Painter, T. H.:
- 14 Satellite-Based Estimation of Temporally Resolved Dust Radiative Forcing in Snow
- 15 Cover, *Journal of Hydrometeorology*, 17, 1999-2011, 2016.
- 16 Nagorski, S. A., Kaspari, S. D., Hood, E., Fellman, J. B., and Skiles, S. M.: Radiative
- 17 Forcing by Dust and Black Carbon on the Juneau Icefield, Alaska, *Journal of*
- 18 *Geophysical Research: Atmospheres*, 124, 3943-3959, 10.1029/2018jd029411, 2019.
- 19 Negi, H. S., and Kokhanovsky, A.: Retrieval of snow grain size and albedo of western
- 20 Himalayan snow cover using satellite data, *The Cryosphere*, 5, 831-847, 10.5194/tc-5-



- 1 831-2011, 2011.
- 2 Nolin, A. W., and Dozier, J.: Estimating snow grain size using AVIRIS data, Remote  
3 Sensing of Environment, 44, 231-238, 10.1016/0034-4257(93)90018-s, 1993.
- 4 Nolin, A. W., and Dozier, J.: A Hyperspectral Method for Remotely Sensing the Grain  
5 Size of Snow, Remote Sensing of Environment, 74, 207-216, 10.1016/s0034-  
6 4257(00)00111-5, 2000.
- 7 Nowottnick, E., Colarco, P., Ferrare, R., Chen, G., Ismail, S., Anderson, B., and Browell,  
8 E.: Online simulations of mineral dust aerosol distributions: Comparisons to NAMMA  
9 observations and sensitivity to dust emission parameterization, Journal of Geophysical  
10 Research, 115, 10.1029/2009jd012692, 2010.
- 11 Nowottnick, E., Colarco, P., da Silva, A., Hlavka, D., and McGill, M.: The fate of  
12 saharan dust across the atlantic and implications for a central american dust barrier,  
13 Atmospheric Chemistry and Physics, 11, 8415-8431, 10.5194/acp-11-8415-2011, 2011.
- 14 Oaida, C. M., Xue, Y., Flanner, M. G., Skiles, S. M., De Sales, F., and Painter, T. H.:  
15 Improving snow albedo processes in WRF/SSiB regional climate model to assess  
16 impact of dust and black carbon in snow on surface energy balance and hydrology over  
17 western U.S, Journal of Geophysical Research: Atmospheres, 120, 3228-3248,  
18 10.1002/2014jd022444, 2015.
- 19 Painter, T. H., Roberts, D. A., Green, R. O., and Dozier, J.: The Effect of Grain Size on  
20 Spectral Mixture Analysis of Snow-Covered Area from AVIRIS Data, Remote Sensing



- 1 of Environment, 65, 320-332, 10.1016/s0034-4257(98)00041-8, 1998.
- 2 Painter, T. H., Barrett, A. P., Landry, C. C., Neff, J. C., Cassidy, M. P., Lawrence, C. R.,  
3 McBride, K. E., and Farmer, G. L.: Impact of disturbed desert soils on duration of  
4 mountain snow cover, Geophysical Research Letters, 34, 10.1029/2007gl030284, 2007.
- 5 Painter, T. H., Rittger, K., McKenzie, C., Slaughter, P., Davis, R. E., and Dozier, J.:  
6 Retrieval of subpixel snow covered area, grain size, and albedo from MODIS, Remote  
7 Sensing of Environment, 113, 868-879, 10.1016/j.rse.2009.01.001, 2009.
- 8 Painter, T. H., Deems, J. S., Belnap, J., Hamlet, A. F., Landry, C. C., and Udall, B.:  
9 Response of Colorado River runoff to dust radiative forcing in snow, Proc Natl Acad  
10 Sci U S A, 107, 17125-17130, 10.1073/pnas.0913139107, 2010.
- 11 Painter, T. H., Bryant, A. C., and Skiles, S. M.: Radiative forcing by light absorbing  
12 impurities in snow from MODIS surface reflectance data, Geophysical Research  
13 Letters, 39, n/a-n/a, 10.1029/2012gl052457, 2012a.
- 14 Painter, T. H., Skiles, S. M., Deems, J. S., Bryant, A. C., and Landry, C. C.: Dust  
15 radiative forcing in snow of the Upper Colorado River Basin: 1. A 6 year record of  
16 energy balance, radiation, and dust concentrations, Water Resources Research, 48,  
17 10.1029/2012wr011985, 2012b.
- 18 Painter, T. H., Seidel, F. C., Bryant, A. C., McKenzie Skiles, S., and Rittger, K.: Imaging  
19 spectroscopy of albedo and radiative forcing by light-absorbing impurities in mountain  
20 snow, Journal of Geophysical Research: Atmospheres, 118, 9511-9523,



- 1 10.1002/jgrd.50520, 2013.
- 2 Pu, W., Wang, X., Wei, H., Zhou, Y., Shi, J., Hu, Z., Jin, H., and Chen, Q.: Properties  
3 of black carbon and other insoluble light-absorbing particles in seasonal snow of  
4 northwestern China, *The Cryosphere*, 11, 1213-1233, 10.5194/tc-11-1213-2017, 2017.
- 5 Pu, W., Cui, J., Shi, T., Zhang, X., He, C., and Wang, X.: The remote sensing of radiative  
6 forcing by light-absorbing particles (LAPs) in seasonal snow over northeastern China,  
7 *Atmospheric Chemistry and Physics*, 19, 9949-9968, 10.5194/acp-19-9949-2019, 2019.
- 8 Qi, L., Li, Q., Henze, D. K., Tseng, H.-L., and He, C.: Sources of springtime surface  
9 black carbon in the Arctic: an adjoint analysis for April 2008, *Atmospheric Chemistry  
10 and Physics*, 17, 9697-9716, 10.5194/acp-17-9697-2017, 2017.
- 11 Qian, Y., Gustafson, W. I., Leung, L. R., and Ghan, S. J.: Effects of soot-induced snow  
12 albedo change on snowpack and hydrological cycle in western United States based on  
13 *Weather Research and Forecasting chemistry and regional climate simulations*, *Journal  
14 of Geophysical Research*, 114, 10.1029/2008jd011039, 2009.
- 15 Qian, Y., Flanner, M. G., Leung, L. R., and Wang, W.: Sensitivity studies on the impacts  
16 of Tibetan Plateau snowpack pollution on the Asian hydrological cycle and monsoon  
17 climate, *Atmospheric Chemistry and Physics*, 11, 1929-1948, 10.5194/acp-11-1929-  
18 2011, 2011.
- 19 Qian, Y., Wang, H., Zhang, R., Flanner, M. G., and Rasch, P. J.: A sensitivity study on  
20 modeling black carbon in snow and its radiative forcing over the Arctic and Northern





- 1 China, *Environmental Research Letters*, 9, 064001, 10.1088/1748-9326/9/6/064001,  
2 2014.
- 3 Qian, Y., Yasunari, T. J., Doherty, S. J., Flanner, M. G., Lau, W. K. M., Ming, J., Wang,  
4 H., Wang, M., Warren, S. G., and Zhang, R.: Light-absorbing particles in snow and ice:  
5 Measurement and modeling of climatic and hydrological impact, *Advances in*  
6 *Atmospheric Sciences*, 32, 64-91, 10.1007/s00376-014-0010-0, 2015.
- 7 Ramanathan, V., and Carmichael, G.: Global and regional climate changes due to black  
8 carbon, *Nature Geoscience*, 1, 221-227, 10.1038/ngeo156, 2008.
- 9 Randles, C. A., da Silva, A. M., Buchard, V., Colarco, P. R., Darmenov, A., Govindaraju,  
10 R., Smirnov, A., Holben, B., Ferrare, R., Hair, J., Shinozuka, Y., and Flynn, C. J.: The  
11 MERRA-2 Aerosol Reanalysis, 1980 Onward. Part I: System Description and Data  
12 Assimilation Evaluation, *Journal of Climate*, 30, 6823-6850, 10.1175/jcli-d-16-0609.1,  
13 2017.
- 14 Ricchiazzi, P., Yang, S., Gautier, C., and Sowle, D.: SBDART: A Research and Teaching  
15 Software Tool for Plane-Parallel Radiative Transfer in the Earth's Atmosphere, *Bulletin*  
16 *of the American Meteorological Society*, 79, 2101-2114, 10.1175/1520-  
17 0477(1998)079<2101:sarats>2.0.co;2, 1998.
- 18 Rittger, K., Painter, T. H., and Dozier, J.: Assessment of methods for mapping snow  
19 cover from MODIS, *Advances in Water Resources*, 51, 367-  
20 380, 10.1016/j.advwatres.2012.03.002, 2013.



- 1 Sarangi, C., Qian, Y., Rittger, K., Bormann, K. J., Liu, Y., Wang, H., Wan, H., Lin, G.,  
2 and Painter, T. H.: Impact of light-absorbing particles on snow albedo darkening and  
3 associated radiative forcing over high-mountain Asia: high-resolution WRF-Chem  
4 modeling and new satellite observations, *Atmospheric Chemistry and Physics*, 19,  
5 7105-7128, 10.5194/acp-19-7105-2019, 2019.
- 6 Seidel, F. C., Rittger, K., Skiles, S. M., Molotch, N. P., and Painter, T. H.: Case study  
7 of spatial and temporal variability of snow cover, grain size, albedo and radiative  
8 forcing in the Sierra Nevada and Rocky Mountain snowpack derived from imaging  
9 spectroscopy, *The Cryosphere*, 10, 1229-1244, 10.5194/tc-10-1229-2016, 2016.
- 10 Siegmund, A. and Menz, G.: Fernes nah gebracht–Satelliten-undLuftbildeinsatz zur  
11 Analyse von Umweltveränderungen im Geographieunterricht, *Geographie und Schule*,  
12 154, 2–10, 2005.
- 13 Skamarock, W. C., Klemp, J. B., Dudhia, J., Gill, D. O., Barker, D. M., Duda, M. G.,  
14 Huang, X., Wang, W., and Powers, J. G.: A description of the advanced research WRF  
15 version 3, NCAR Tech. Note, NCAR/TN-475+STR, 8 pp., Natl. Cent. for Atmos. Res.,  
16 Boulder, Colo., 2008 (available at:  
17 [http://www.mmm.ucar.edu/wrf/users/docs/arw\\_v3.pdf](http://www.mmm.ucar.edu/wrf/users/docs/arw_v3.pdf))
- 18 Skiles, S. M., and Painter, T.: Daily evolution in dust and black carbon content, snow  
19 grain size, and snow albedo during snowmelt, Rocky Mountains, Colorado, *J Glaciol*,  
20 63, 118-132, 10.1017/jog.2016.125, 2016.



- 1 Skiles, S. M., Flanner, M., Cook, J. M., Dumont, M., and Painter, T. H.: Radiative  
2 forcing by light-absorbing particles in snow, *Nature Climate Change*, 8, 964-971,  
3 10.1038/s41558-018-0296-5, 2018.
- 4 Solomos, S., Ansmann, A., Mamouri, R.-E., Biniotoglou, I., Patlakas, P., Marinou, E.,  
5 and Amiridis, V.: Remote sensing and modelling analysis of the extreme dust storm  
6 hitting the Middle East and eastern Mediterranean in September 2015, *Atmospheric  
7 Chemistry and Physics*, 17, 4063-4079, 10.5194/acp-17-4063-2017, 2017.
- 8 Stamnes, K., Tsay, S. C., Wiscombe, W., and Jayaweera, K.: Numerically stable  
9 algorithm for discrete-ordinate-method radiative transfer in multiple scattering and  
10 emitting layered media, *Appl Opt*, 27, 2502-2509, 10.1364/AO.27.002502, 1988.
- 11 Sterle, K. M., McConnell, J. R., Dozier, J., Edwards, R., and Flanner, M. G.: Retention  
12 and radiative forcing of black carbon in eastern Sierra Nevada snow, *The Cryosphere*,  
13 7, 365-374, 10.5194/tc-7-365-2013, 2013.
- 14 Sturm, M., Holmgren, J., and Liston, G. E.: A Seasonal Snow Cover Classification  
15 System for Local to Global Applications, *Journal of Climate*, 8, 1261-1283,  
16 10.1175/1520-0442(1995)008<1261:assccs>2.0.co;2, 1995.
- 17 Su, W., Corbett, J., Eitzen, Z., and Liang, L.: Next-generation angular distribution  
18 models for top-of-atmosphere radiative flux calculation from CERES instruments:  
19 validation, *Atmospheric Measurement Techniques*, 8, 3297-3313, 10.5194/amt-8-3297-  
20 2015, 2015.



- 1 Tedesco, M., and Kokhanovsky, A. A.: The semi-analytical snow retrieval algorithm  
2 and its application to MODIS data, *Remote Sensing of Environment*, 111, 228-241,  
3 10.1016/j.rse.2007.02.036, 2007.
- 4 Teillet, P. M., Guindon, B., and Goodenough, D. G.: On the Slope-Aspect Correction  
5 of Multispectral Scanner Data, *Canadian Journal of Remote Sensing*, 8, 84-106,  
6 10.1080/07038992.1982.10855028, 1982.
- 7 Toon, O. B., McKay, C. P., Ackerman, T. P., and Santhanam, K.: Rapid calculation of  
8 radiative heating rates and photodissociation rates in inhomogeneous multiple  
9 scattering atmospheres, *Journal of Geophysical Research*, 94, 16287,  
10 10.1029/JD094iD13p16287, 1989.
- 11 Wang, H. L., Rasch, P. J., Easter, R. C., Singh, B., Zhang, R. D., Ma, P. L., Qian, Y.,  
12 Ghan, S. J., and Beagley, N.: Using an explicit emission tagging method in global  
13 modeling of source-receptor relationships for black carbon in the Arctic: Variations,  
14 sources, and transport pathways, *J Geophys Res-Atmos*, 119, 12888-12909, 2014a.
- 15 Wang, R., Tao, S., Shen, H., Wang, X., Li, B., Shen, G., Wang, B., Li, W., Liu, X.,  
16 Huang, Y., Zhang, Y., Lu, Y., and Ouyang, H.: Global emission of black carbon from  
17 motor vehicles from 1960 to 2006, *Environ Sci Technol*, 46, 1278-1284,  
18 10.1021/es2032218, 2012.
- 19 Wang, R., Tao, S., Ciais, P., Shen, H. Z., Huang, Y., Chen, H., Shen, G. F., Wang, B.,  
20 Li, W., Zhang, Y. Y., Lu, Y., Zhu, D., Chen, Y. C., Liu, X. P., Wang, W. T., Wang, X. L.,



- 1 Liu, W. X., Li, B. G., and Piao, S. L.: High-resolution mapping of combustion processes  
2 and implications for CO<sub>2</sub> emissions, *Atmospheric Chemistry and Physics*, 13, 5189-  
3 5203, 10.5194/acp-13-5189-2013, 2013a.
- 4 Wang, R., Tao, S., Shen, H., Huang, Y., Chen, H., Balkanski, Y., Boucher, O., Ciais, P.,  
5 Shen, G., Li, W., Zhang, Y., Chen, Y., Lin, N., Su, S., Li, B., Liu, J., and Liu, W.: Trend  
6 in global black carbon emissions from 1960 to 2007, *Environ Sci Technol*, 48, 6780-  
7 6787, 10.1021/es5021422, 2014b.
- 8 Wang, X., Doherty, S. J., and Huang, J.: Black carbon and other light-absorbing  
9 impurities in snow across Northern China, *Journal of Geophysical Research:*  
10 *Atmospheres*, 118, 1471-1492, 10.1029/2012jd018291, 2013b.
- 11 Wang, X., Pu, W., Ren, Y., Zhang, X., Zhang, X., Shi, J., Jin, H., Dai, M., and Chen, Q.:  
12 Observations and model simulations of snow albedo reduction in seasonal snow due to  
13 insoluble light-absorbing particles during 2014 Chinese survey, *Atmospheric*  
14 *Chemistry and Physics*, 17, 2279-2296, 10.5194/acp-17-2279-2017, 2017.
- 15 Warren, S. G.: Optical properties of snow, *Reviews of Geophysics*, 20, 67,  
16 10.1029/RG020i001p00067, 1982.
- 17 Warren, S. G.: Impurities in Snow: Effects on Albedo and Snowmelt (Review), *Annals*  
18 *of Glaciology*, 5, 177-179, 10.3189/1984AoG5-1-177-179, 1984.
- 19 Warren, S. G., and Brandt, R. E.: Optical constants of ice from the ultraviolet to the  
20 microwave: A revised compilation, *Journal of Geophysical Research*, 113,

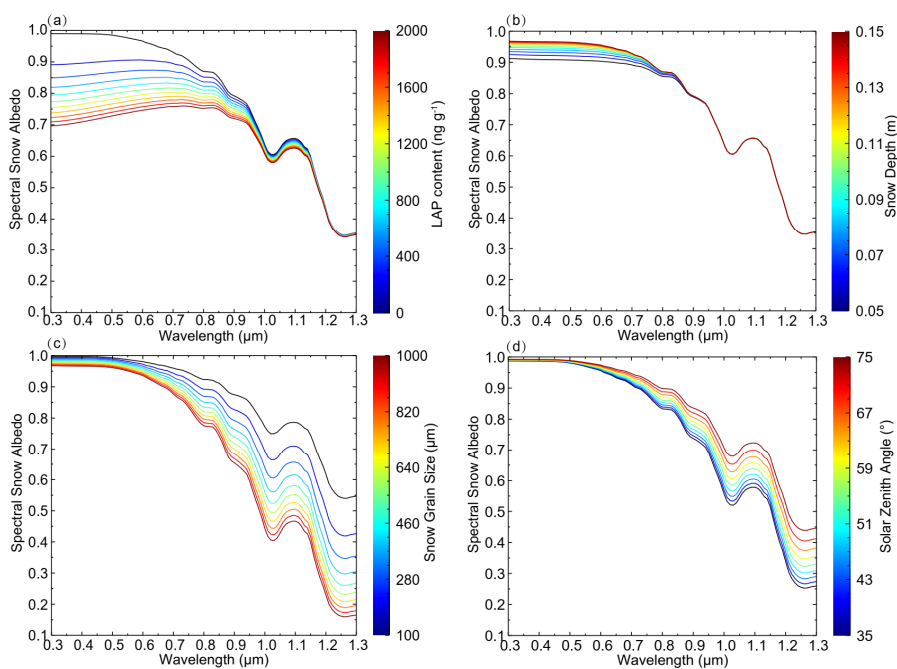


- 1 10.1029/2007jd009744, 2008.
- 2 Warren, S. G.: Can black carbon in snow be detected by remote sensing?, Journal of  
3 Geophysical Research: Atmospheres, 118, 779-786, 10.1029/2012jd018476, 2013.
- 4 Wiscombe, W. J., and Warren, S. G.: A Model for the Spectral Albedo of Snow. I: Pure  
5 Snow, Journal of the Atmospheric Sciences, 37, 2712-2733, 10.1175/1520-  
6 0469(1980)037<2712:amftsa>2.0.co;2, 1980.
- 7 Ye, H., Zhang, R., Shi, J., Huang, J., Warren, S. G., and Fu, Q.: Black carbon in seasonal  
8 snow across northern Xinjiang in northwestern China, Environmental Research Letters,  
9 7, 044002, 10.1088/1748-9326/7/4/044002, 2012.
- 10 Zhao, C., Hu, Z., Qian, Y., Ruby Leung, L., Huang, J., Huang, M., Jin, J., Flanner, M.  
11 G., Zhang, R., Wang, H., Yan, H., Lu, Z., and Streets, D. G.: Simulating black carbon  
12 and dust and their radiative forcing in seasonal snow: a case study over North China  
13 with field campaign measurements, Atmospheric Chemistry and Physics, 14, 11475-  
14 11491, 10.5194/acp-14-11475-2014, 2014.
- 15 Zhong, E., Li, Q., Sun, S., Chen, S., and Chen, W.: Analysis of euphotic depth in snow  
16 with SNICAR transfer scheme, Atmospheric Science Letters, 18, 484-490,  
17 10.1002/asl.792, 2017.
- 18 Zhu, C., Kobayashi, H., Kanaya, Y., and Saito, M.: Size-dependent validation of  
19 MODIS MCD64A1 burned area over six vegetation types in boreal Eurasia: Large  
20 underestimation in croplands, Sci Rep, 7, 4181, 10.1038/s41598-017-03739-0, 2017.



1

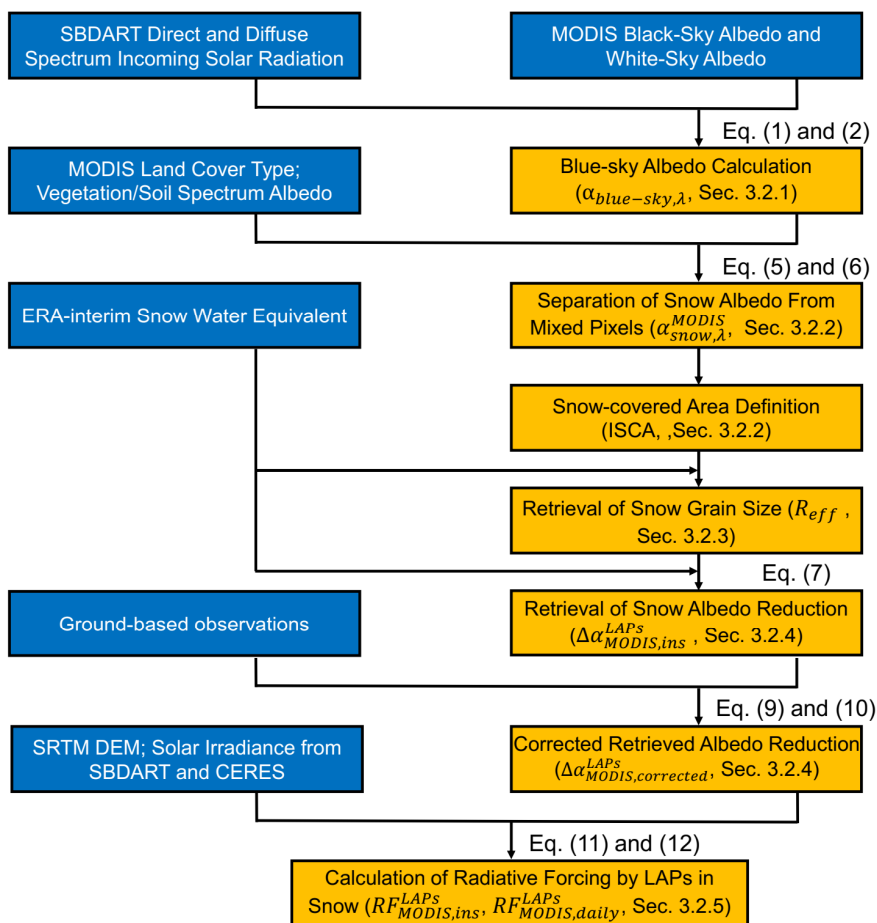
2



3

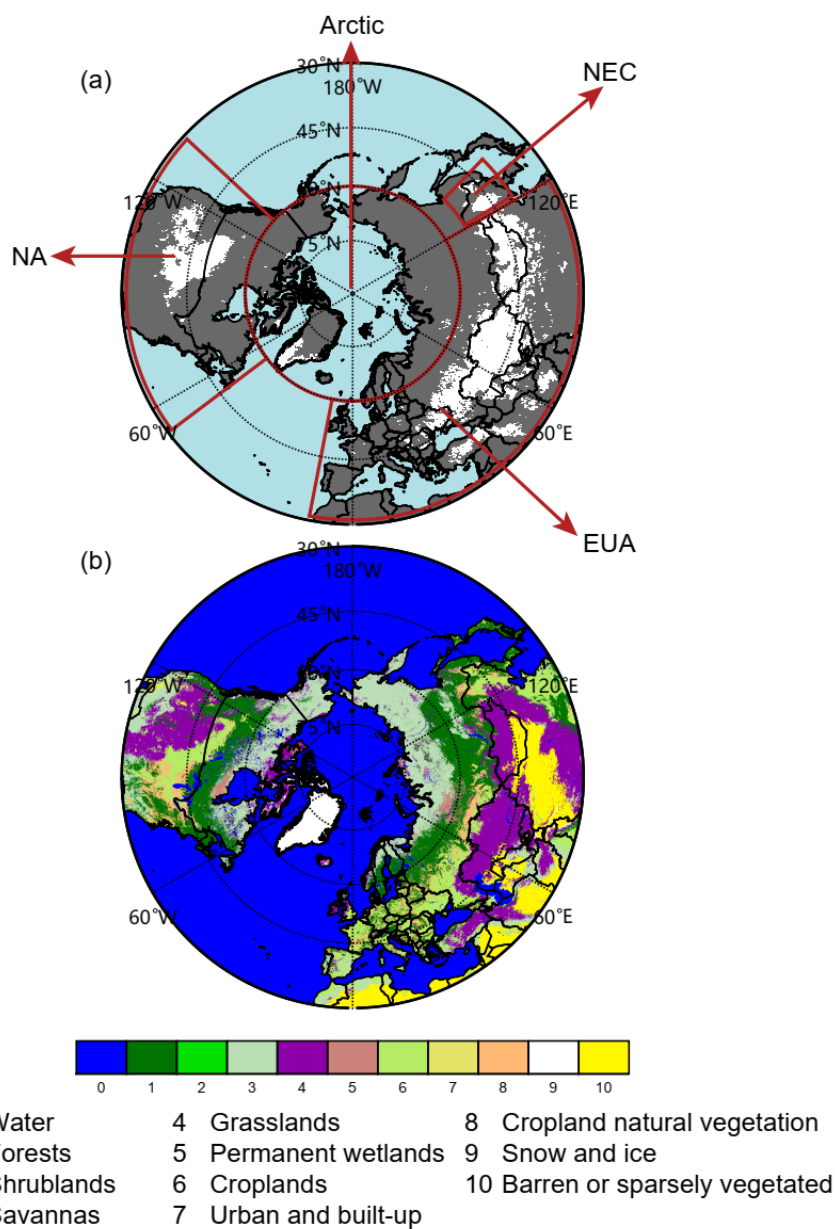
4 Figure 1. Variations in spectral snow albedo due to (a) LAP content ( $\text{ng g}^{-1}$ ), (b) snow depth (m), (c)  
5 snow grain size ( $\mu\text{m}$ ), and (d) solar zenith angle ( $\text{deg}$ ).

6

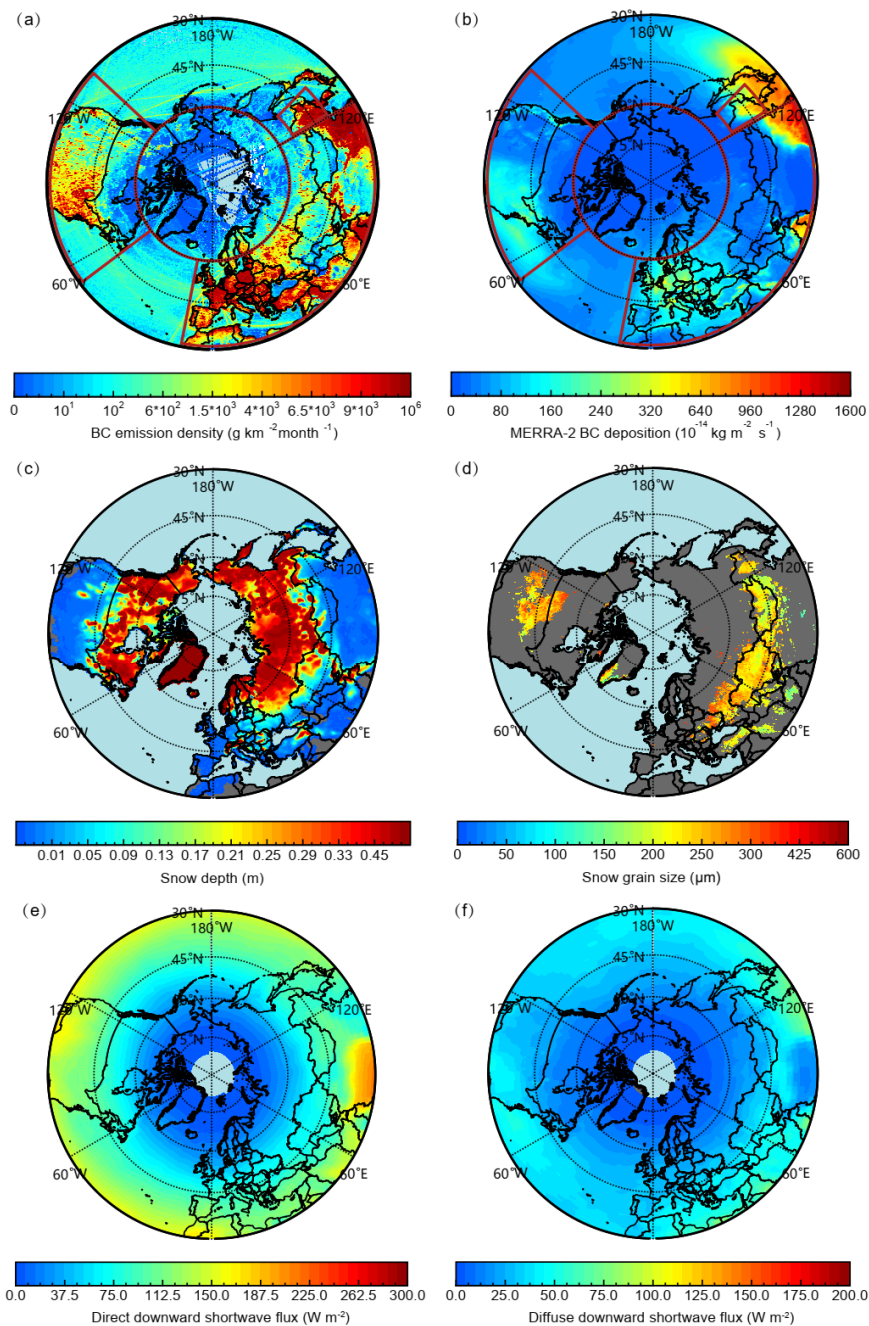


1  
 2 Figure 2. Workflow depicting the calculation and validation of radiative forcing of LAPs in snow:  
 3 the blue boxes denote the external input data, while the orange boxes are used for calculations in  
 4 this study.





1  
 2 Figure 3. Spatial distributions of (a) identified snow-covered areas (ISCA) and (b) the different land-  
 3 cover types, based on MODIS data, for the Northern Hemisphere. ISCA (white) can be separated  
 4 into northeastern China (NEC), Eurasia (EUA), North America (NA), and the Arctic.



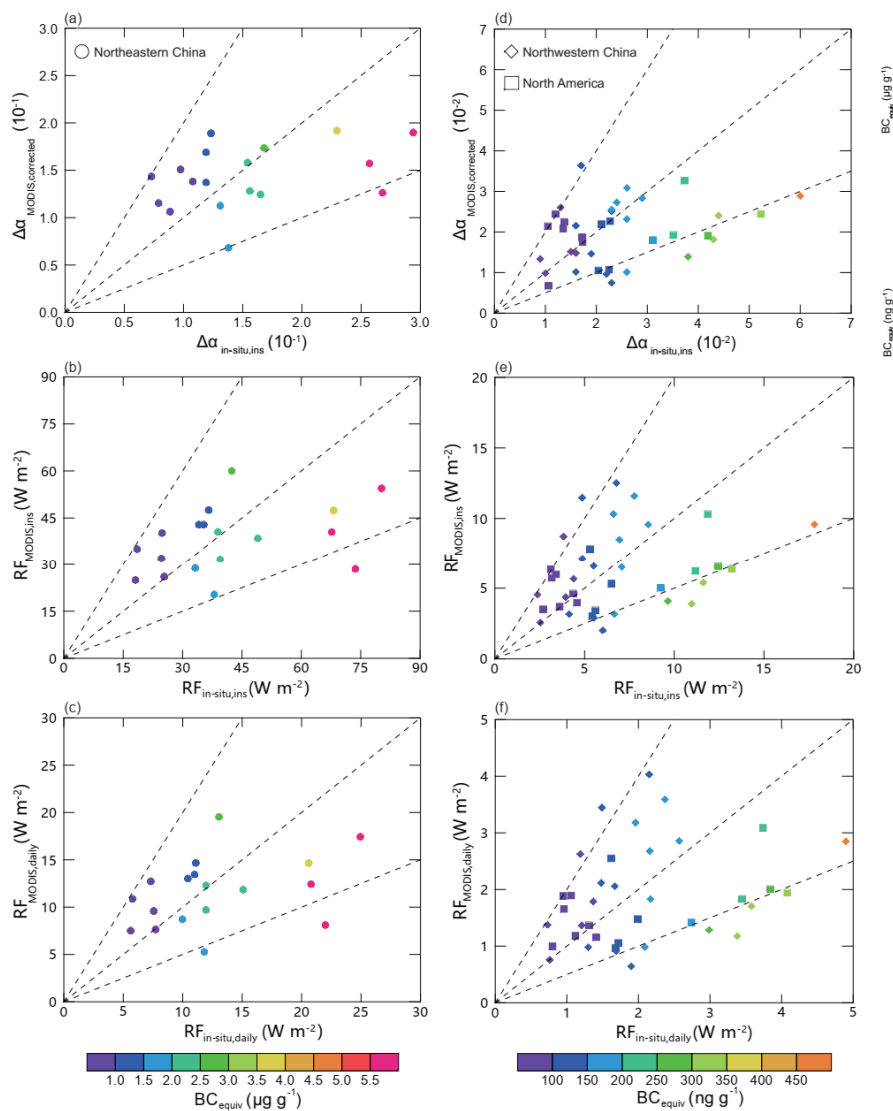
1  
2 Figure 4. Spatial distributions of average (a) BC emissions density, (b) BC deposition from  
3 MERRA-2, (c) snow depth from ERA-interim, (d) snow grain size retrieved by MODIS, (e) direct  
4 and (f) diffuse solar irradiance at the surface in January–February from CERES. BC emissions



- 1 density is for the period 2003–2014 and employs data from the research group at Peking University,
- 2 with additional data collected between 2003 and 2018.
- 3

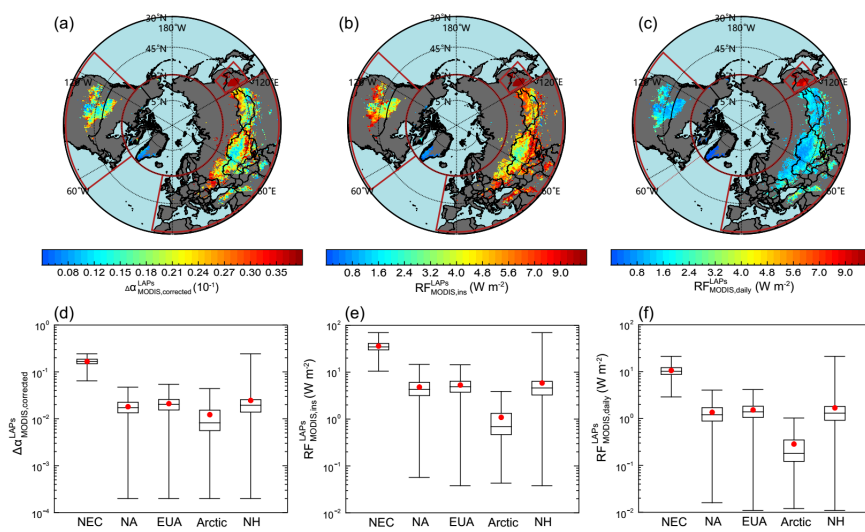


1



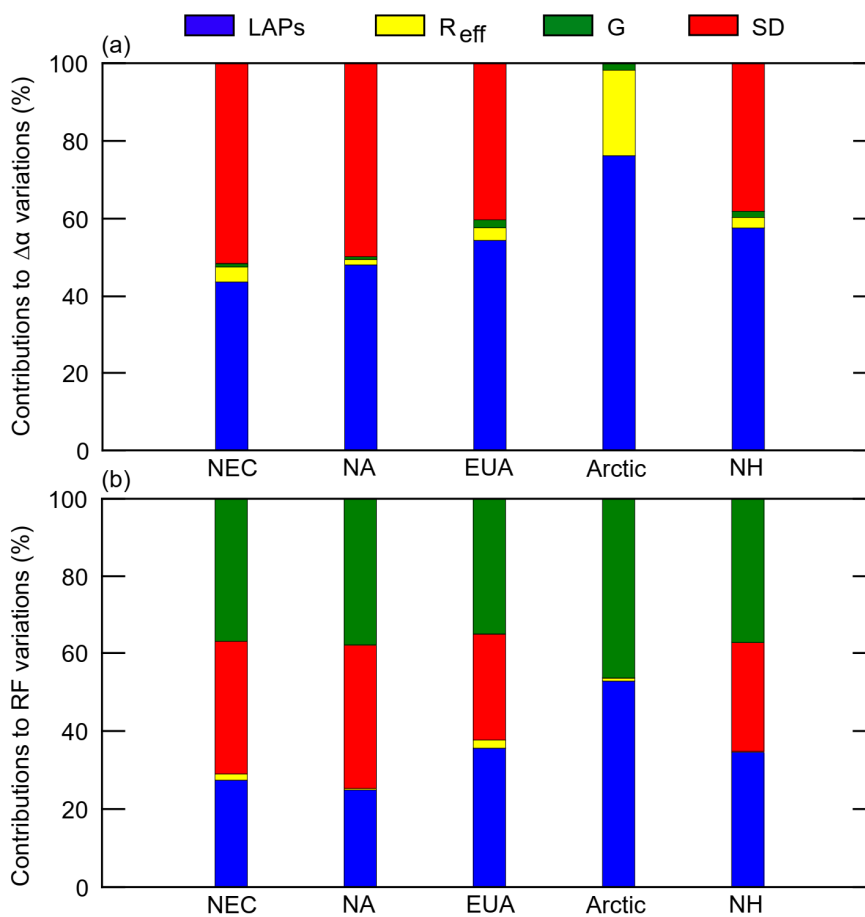
2

3 Figure 5. Scatterplots of (a)  $\Delta\alpha_{MODIS,corrected}$  versus  $\Delta\alpha_{in-situ,ins}$ , (b)  $RF_{MODIS,ins}$  versus  
 4  $RF_{in-situ,ins}$ , and (c)  $RF_{MODIS,daily}$  versus  $RF_{in-situ,daily}$  in heavily polluted areas. Panels (d)–  
 5 (f) illustrate the same scatterplots as in (a)–(c) but for slightly polluted regions. Circles, diamonds,  
 6 and squares represent the snow samples collected in NEC, NWC, and NA, respectively.



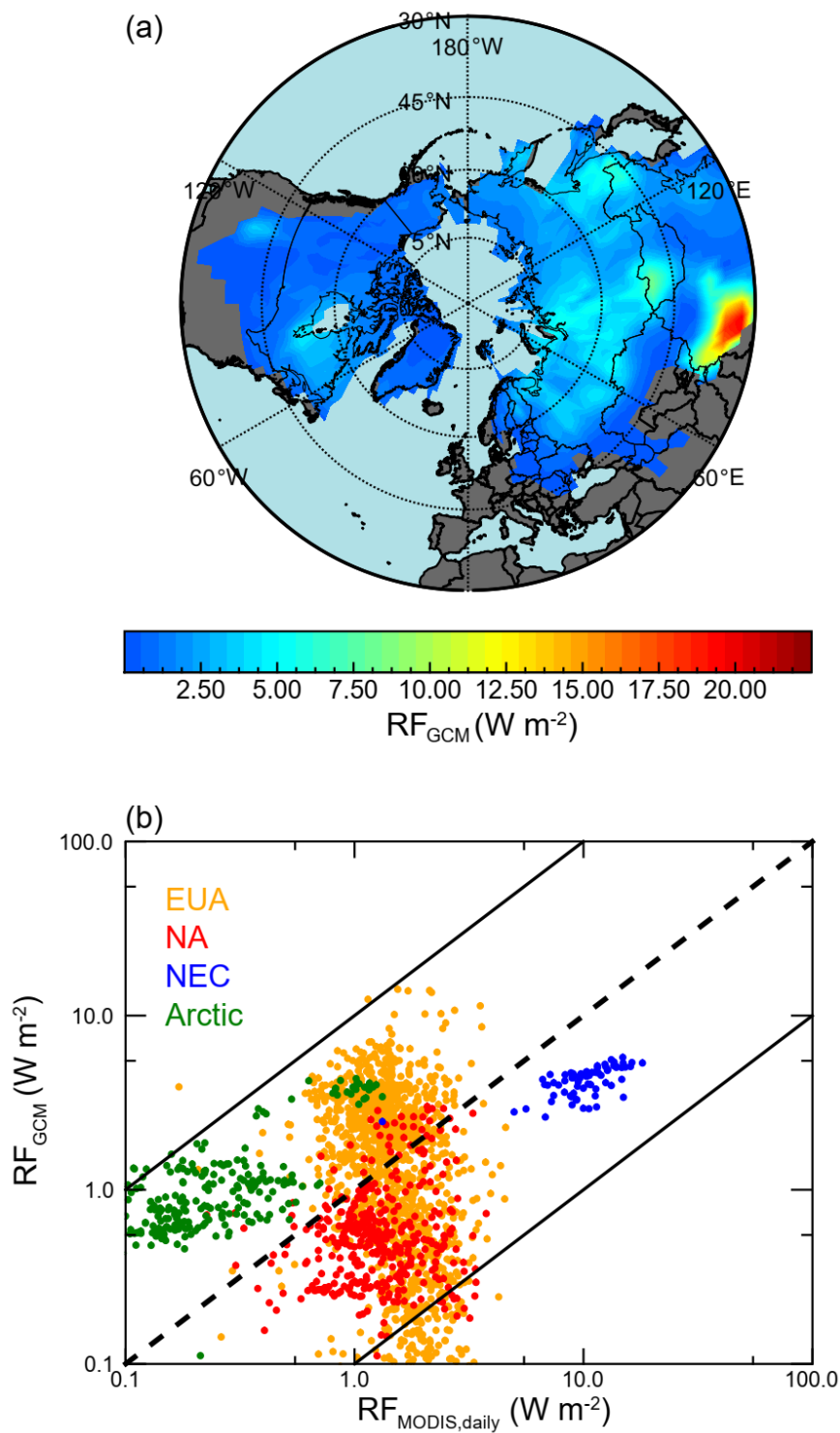
1

2 Figure 6. Spatial distributions of averaged (a)  $\Delta\alpha_{MODIS,corrected}$ , (b)  $RF_{MODIS,ins}$ , and (c)  
 3  $RF_{MODIS,daily}$  and statistics for regionally averaged (d)  $\Delta\alpha_{MODIS,corrected}$ , (e)  $RF_{MODIS,ins}$ , and (f)  
 4  $RF_{MODIS,daily}$  for the Northern Hemisphere in January–February during the period 2003–2018. The  
 5 boxes denote the 25th and 75th quantiles, and the horizontal lines represent the 50th quantiles  
 6 (medians), the averages are shown as red dots; the whiskers denote the 5th and 95th quantiles.



1

2 Figure 7. Fractional contributions of LAPs, snow grain size ( $R_{eff}$ ), geographic factor ( $G$ ), and snow  
3 depth ( $SD$ ) to the spatial variations of (a) snow albedo reduction and (b) radiative forcing.



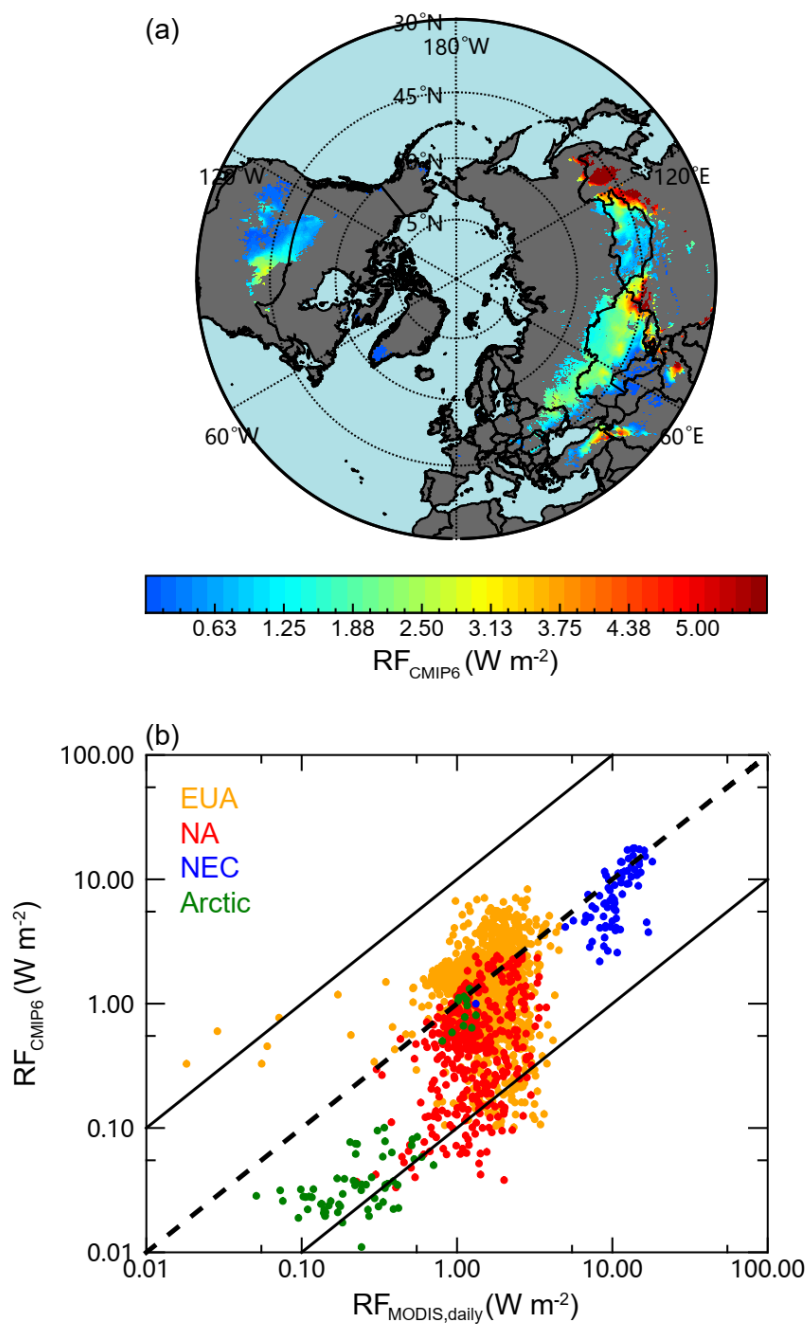


- 1 Figure 8. Spatial distributions of (a) springtime radiative forcing ( $RF_{GCM}$ ) due to LAPs in snow,
- 2 derived from a GCM run by Flanner et al. (2007), and scatterplot of (b)  $RF_{MODIS,daily}$  versus
- 3  $RF_{GCM}$ .
- 4





1



2

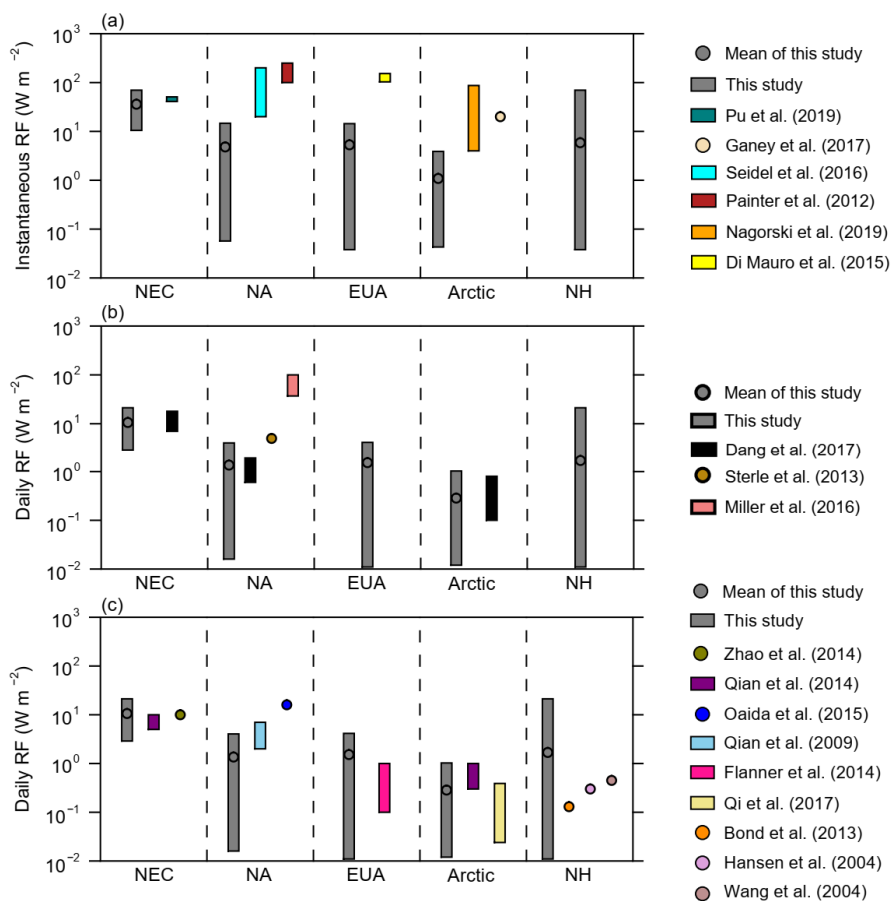
3 Figure 9. (a) Spatial distributions of average-daily radiative forcing ( $RF_{CMIP6}$ ), based on the CMIP6



- 1 ensemble-average soot content of snow in January–February for the period 2003–2014. (b)
- 2 Scatterplot of  $RF_{MODIS,daily}$  versus  $RF_{CMIP6}$ .
- 3



1



2

3 Figure 10. Comparisons of radiative forcing due to LAPs in snow (this study) with observed and  
 4 model-simulated values from previous studies.

5

6

7

8

9

10